Master of Science Thesis

Identification of Momentum Forcing Required to Reduce Base-Model Errors Using Full-Field Inversion

Woosik Yoon

February 20, 2017

Faculty of Aerospace Engineering

Delft University of Technology

Identification of Momentum Forcing Required to Reduce Base-Model Errors Using Full-Field Inversion

Master of Science Thesis

For obtaining the degree of Master of Science in Aerospace Engineering
at Delft University of Technology

Woosik Yoon

February 20, 2017

Faculty of Aerospace Engineering · Delft University of Technology

Delft University of Technology

DELFT UNIVERSITY OF TECHNOLOGY
DEPARTMENT OF AERODYNAMICS

The undersigned hereby certify that they have read and recommend to the Faculty of Aerospace Engineering for acceptance the thesis entitled **“Identification of Momentum Forcing Required to Reduce Base-Model Errors Using Full-Field Inversion”** by **Woosik Yoon** in fulfillment of the requirements for the degree of **Master of Science**.

Dated: February 20, 2017

Supervisors:

Dr.ir. M.I. Gerritsma

Dr. R.P. Dwight

Dr. D. Ragni

M. Schmelzer, MSc

Summary

Reynolds Averaged Navier-Stokes turbulence models have been widely used in many industrial applications because of their lower computational cost compared to other simulation approaches such as DNS and LES. This is a consequence of considering mean-flow quantities achieved by the time-averaging process. However, the time-averaging introduces the Reynolds stresses, which make the system of the RANS equations underdetermined, thus requiring modelling approaches. As a consequence of modelling the Reynolds stresses based on the Boussinesq hypothesis, RANS simulations contain model errors. To improve the RANS predictive capability, this thesis aims to identify momentum forcing $\mathbf{f}$ that is required to reduce base-model errors with respect to any given data, and determine its characteristics.

The literature study on existing RANS error estimation techniques concludes two major approaches. The Bayesian approach improves the RANS predictions by calibrating the closure coefficients of the RANS models. The turbulence production is iteratively corrected based on the estimated functional errors by the full-field inversion. However, since both approaches still rely on the Boussinesq hypothesis, they do not provide the improvement where the turbulent anisotropy plays a role.

To avoid the Boussinesq approximation, a base-model is constructed by replacing the divergence of the Reynolds stress tensor with the momentum forcing $\mathbf{f}$. By performing the full-field inversion, optimal momentum forcing $\hat{\mathbf{f}}$ is identified based on the mean DNS velocity data for two different wall-bounded flow cases. The velocity difference between the base-model and the mean DNS velocity data is significantly reduced by achieving $\mathbf{f} = \hat{\mathbf{f}}$ for both test cases. Furthermore, the flow separation and reattachment points are accurately estimated by only correcting the velocity field.

The identified momentum forcing $\hat{\mathbf{f}}$ mostly agrees with the DNS turbulence force for the 1D channel flow case, while some deviations of $\hat{\mathbf{f}}$ from the DNS turbulence force are observed due to the flow separation in the 2D periodic hill flow case. To determine the characteristics of $\hat{\mathbf{f}}$, a shear stress component is extracted from $\hat{\mathbf{f}}$ and compared with the DNS Reynolds shear stress. In the 1D channel flow case, the shear stress is directly determined by integrating $\hat{\mathbf{f}}$ along the cross-section of the channel and matches with the DNS Reynolds shear stress. On the other hand, the direct extraction of the shear stress turns out to be not possible for the 2D periodic hill flow case, hence using a minimization approach. Together with the flow separation, this lead to the deviations in the shear stress profiles.

Table of Contents

List of Figures

List of Tables

Chapter 1

Introduction

Many different techniques have been proposed to perform more efficient and accurate turbulence computations in the field of computational fluid dynamics (CFD) (Pope, 2000). The full scale turbulence computation is made by Direct Numerical Simulation (DNS). This is known as the most accurate technique but requires large computational costs. Large Eddy Simulation (LES) has been developed to reduce the computational cost by filtering the small length scales of the turbulence. Both techniques still have some limitations in practical engineering applications particularly for high Reynolds number flows bounded by complex geometries due to the large computational cost. Many engineering turbulence predictions rely on Reynolds-Averaged Navier-Stokes (RANS) simulations where the computational cost is significantly reduced by modelling turbulent transport instead of resolving the full scales of the turbulence. However, the RANS simulations involves the errors from the turbulence model and its empirical parameters, thus yielding inaccurate turbulence predictions.

Different error estimation techniques have been developed to improve the RANS predictive capability. A full-field inversion approach is one of the promising techniques in the field of RANS uncertainty quantification. This is a data-driven approach which can inversely find the optimal estimate of the quantity of interest by minimizing the difference in the full flow field between the RANS simulation and a selected database. Parish and Duraisamy (2015) applied this approach to correct the turbulence production of the RANS closure model. In contrast to their work, this thesis exploits the full-field inversion technique to reproduce the momentum forcing necessary to reduce the errors of a base-model in specific test cases. To consolidate the purpose of the thesis, the introduction will start with the state-of-the art and address the motivation of this research and a brief summary of the approach used. Then, research questions will be defined and followed by the outline of the thesis.

1.1 State-of-the-art

1.1.1 Bayesian approach

To begin with, Kennedy and OHagan (2001) initially introduced a methodology of Bayesian calibration for computer models. They defined the calibration as the process where a model output was achieved to agree with observation data by adjusting model parameters. The proposed Bayesian technique contains the predictions regarding all sources of uncertainty as well as correction for inaccurate outputs of the model. Cheung et al. (2011) applied the Bayesian technique to perform the calibration process of different stochastic model classes based on the SpalartAllmaras (SA) turbulence model. The calibration process was performed against the incompressible flat plate boundary layer experiment data. The resulted posterior probabilities and the prediction for the quantities of interest were used to determine the plausibility of the selected stochastic model class. Their result concluded that there was only one stochastic model case that is plausible for the prediction while other two are rejected.

Oliver and Moser (2011) continued applying the Bayesian uncertainty quantification technique to different RANS turbulence models for fully-developed channel flow. In the work, they aimed to quantify both parameter and model-form uncertainties of various RANS models: Baldwin-Lomax (BL), SpalartAllmaras (SA), Chien $k-\epsilon$ and v^2-f. The result shows that the maximum posteriors of the SA parameters are nearest to their nominal values among other turbulence models while the Chien $k-\epsilon$ requires a larger parameter value than its nominal value to be agreed with the calibration data. The Chien $k-\epsilon$ model is coupled with different stochastic models to predict the quantity of interest. The predictions are shown to be significantly influenced by the stochastic model and provide no agreement among the data set. On the other hand, when one of the stochastic extensions is coupled with the different turbulence models, the plausible predictions are achieved except for the BL model.

Edeling et al. (2014) further investigated parameter variability in $k-\epsilon$ turbulence model by using Bayesian uncertainty analysis for the case of turbulent boundary layers with different pressure gradients. Based on experiment data, the closure coefficients for the turbulence model were calibrated for different pressure gradient cases. In particular, their work summarized the large number of posteriors through highest posterior-density (HPD) intervals, which represent the variability of closure coefficients and provide information about model-inadequacy. 13 different boundary layer flows were considered and the calibrations were performed for each velocity profile. The result shows that the posteriors of the closure coefficients are either widely spread or not properly identified within a single calibration. This indicates that it is insufficient to obtain steady estimate of model discrepancies by performing a single calibration. However, the later result produced based on 13 calibrations gives the closure error estimate that is consistent with the given experiment data.

1.1.2 Anisotropy perturbation approach

Emory et al. (2011) attempted to estimate RANS model-form uncertainty by introducing uncertainties directly to Reynolds stress tensor. This is a good motivation as the model-form error exists due to the approximated Reynolds stress components. The methodology of this approach is to perturb the eigenvalues of the Reynolds stress anisotropy in order to represent the injected uncertainty. The uncertainty quantification analysis was performed on SST $k - \omega$ turbulence model for the computation of shock/boundary layer interactions. The study shows that the approach of the turbulence anisotropy perturbation is capable of influencing the flow separation in the boundary layer. In addition, nominal predictions are bounded by the resulted anisotropy perturbations. However, the perturbations in their work were only introduced in limited directional components. Therefore, further development regarding the directionality of the perturbations is suggested for its capability of boundedness for any arbitrary directions.

Gorlé et al. (2012) followed the approach of Emory et al. (2011) for the flow over a wavy wall in order to obtain the generalized perturbation functions. The analysis and validation are based on DNS data of the flow over a wavy wall. In their work, a marker was additionally introduced to indicate the region where perturbations need to be injected, thus resulting systematic perturbations in that region. The result of using systematic perturbations indicates that the simulation with a particular directional movement of eigenvalues provides better agreement with the DNS data than the simulations with varying the eigenvalue in other directions.

The framework of the anisotropy perturbation approach was tested by Gorlé and Iaccarino (2013) on a jet supersonic cross flow simulation with a LES database. The perturbation was introduced in the turbulence kinetic energy as well as in the anisotropy eigenvalues in order to investigate the Reynolds stress. The perturbation ranges was determined based on the LES data. A clear distinction was made by the marker that indicates the region of uncertainties. Although they again proved the capability of the marker, the uncertainty over the flow field was not entirely captured. They concluded that this was because the range of LES isolines was not completely bounded by the domain of this framework.

Xiao et al. (2016) combined the anisotropy perturbation approach with the Bayesian framework. They aimed to reduce the model-form uncertainty of the RANS simulations in addition to the quantification. As opposed to the work of Emory et al. (2011), the perturbed anisotropies were considered as random fields. By following the framework of the Bayesian approach, the uncertainties are propagated to the posterior distributions of quantities of interest based on the prior knowledge and observation data. The framework was tested on the periodic hill flow and the square duct flow. However, the study was concluded that the inferred full Reynolds stress tensor fields do not represent the accurate Reynolds stress tensor field.

1.1.3 Adjoint-based inversion approach

An adjoint-based inversion approach was proposed by Wang and Dow (2011) to quantify structural uncertainties in a RANS turbulence model. The aim of their work was to determine the eddy viscosity by minimizing the difference in velocities simulated by RANS and DNS, and model the structural uncertainties based on the obtained the eddy viscosity. The key idea of this approach is to minimize a constructed cost function based on adjoint sensitivities. The adjoint approach has a capability to reduce the enormous computational cost during the optimization. The framework was tested in channel flow with the $k-\omega$ turbulence model. The result shows that the optimal eddy viscosity profile almost is agreed with the eddy viscosity profile extracted from the DNS data, particularly near the wall, while their discrepancies increase as further from the wall.

While Wang and Dow (2011) pursued to obtain the optimal eddy viscosity, Parish and Duraisamy (2015) and Parish and Duraisamy (2016) introduced functional errors directly to the turbulence production term in RANS transport equations. They used the full-field inversion to estimate the optimal functional errors of the turbulence closure models on the turbulent channel flow and the convex/concave wall bounded flow. Using the Bayesian framework, they modelled the DNS dataset based on Gaussian uncertainty. By considering the maximum a posteriori (MAP) estimate of the functional error probability distribution, a deterministic optimization problem was formulated. The adjoint method was used to solve the deterministic optimization problem. Having successfully estimated the deterministic solution of the functional errors, they further applied the machine learning corrections to reconstruct the inferred information.

Singh and Duraisamy (2016) performed the full-field inversion for more complicated flow problems such as turbulent flow with curvature, oblique shock turbulent boundary layer interaction and high angle of attack flow over S809 airfoil in addition to turbulent channel flow. Furthermore, they aimed to achieve realizations of turbulence closure models based on limited data points. The result for the channel flow provides almost the same posterior velocity profile compared to DNS and it was found that an additional time scale correction was required near the wall. Assimilating limited skin-friction data provides more accurate velocity profiles for the flow with curvature. With given wall-pressure data, the prediction of the flow field is well obtained in the oblique shock-turbulent boundary layer interaction case. For the S809 airfoil, limited surface pressure data on a suction side from experiments are used, and accurate predictions are made for the separation as well as lift distributions.

1.2 Motivation and Approach

The success of quantifying the uncertainty of RANS closure coefficients by Edeling et al. (2014) results in practical solutions to the RANS development, by providing statistical information of the closure coefficients. Also, Singh and Duraisamy (2016) improve the RANS turbulence predictions by iteratively correcting the turbulence production based on the functional error estimate. Although both studies have increased the RANS predictive capability by either correcting the closure coefficients or the turbulence production, they still rely on the Boussinesq approximation. Thus, the capability of the existing approaches is still limited for flows in which the turbulent anisotropy plays a role.

As an alternative, a modification can be made on the divergence of the Reynolds stress tensor. The turbulent force is represented by the divergence of the Reynolds stress tensor in the RANS momentum equation. Due to the Boussinesq approximation, the capability of the RANS simulations is limited to provide the accurate predictions for the turbulence force. This thesis aims to estimate the correct turbulence force without modelling the eddy viscosity. To eliminate the contribution of the eddy viscosity, the divergence of the Reynolds stress tensor is replaced by the momentum forcing $\mathbf{f}$. This modification leads to the base-model momentum equation:

$$\rho\nabla \cdot (\bar{\mathbf{u}}\bar{\mathbf{u}}) + \nabla\bar{p} - \nabla \cdot (2\mu D(\bar{\mathbf{u}})) + \mathbf{f} = 0 \tag{1.1}$$

If the momentum forcing $\mathbf{f}$ completely fulfils the turbulence force data $\mathbf{d}$, then the system can be given by

$$\mathbf{H}(\mathbf{f}) = \mathbf{d} \tag{1.2}$$

where $\mathbf{H}(\cdot)$ is the base-model operator. The system (1.2) can be also interpreted that the errors of the base-model $\mathbf{H}$ with respect to the data $\mathbf{d}$ are completely eliminated by imposing the turbulence force to $\mathbf{f}$. However, the momentum forcing $\mathbf{f}$ can not be directly determined since the base-model $\mathbf{H}$ does not have knowledge or information on achieving $\mathbf{d}$, thus requiring an inverse approach.

The inverse approach is the process by which the causes are calculated based on a set of observation data (R. C. Aster and Thurber, 2005). The full-field inversion introduced by Parish and Duraisamy (2015) is capable of providing deterministic estimate of $\mathbf{f}$ by minimizing the difference between $\mathbf{H}(\mathbf{f})$ and $\mathbf{d}$ through the adjoint-based optimization. The framework begins with the Bayesian statistics where the posterior of $\mathbf{f}$ given data $\mathbf{d}$ can be expressed by

$$\mathbf{p}(\mathbf{f}|\mathbf{d}) \propto \mathbf{p}(\mathbf{d}|\mathbf{f})\mathbf{p}_o(\mathbf{f}) \tag{1.3}$$

where $\mathbf{p}(\mathbf{d}|\mathbf{f})$ is the likelihood and $\mathbf{p}_o$ is the prior. The data $\mathbf{d}$ is statistically modelled based on the Gaussian uncertainty $\boldsymbol{\epsilon}_s$ of the base-model such that

$$\mathbf{d} = \mathbf{H}(\mathbf{f}) + \boldsymbol{\epsilon}_s, \qquad \boldsymbol{\epsilon}_s \sim \mathcal{N}(0, \sigma^2_{\boldsymbol{\epsilon}_s}) \tag{1.4}$$

with the standard deviation $\sigma_{\boldsymbol{\epsilon}_s}$. By assuming that the likelihood $\mathbf{p}(\mathbf{d}|\mathbf{f})$ and the prior $\mathbf{p}_o$ are both normally distributed, a deterministic expression for $\mathbf{f}$ can be derived from when the posterior $\mathbf{p}(\mathbf{f}|\mathbf{d})$ is at maximum. As a consequence, the problem (1.2) becomes a deterministic optimization problem.

Solving the deterministic problem is also another challenge when it becomes a high dimensional problem. In the optimization, the momentum forcing $\mathbf{f}$ is considered as a design variable. The dimension of $\mathbf{f}$ increases with the number of control volumes. This means that the optimizer has to deal with the large number of design parameters, thus increasing the computational cost. To resolve the high-dimensional issue, the adjoint-based optimization is used in this thesis. The adjoint method allows to efficiently solve the deterministic optimization problem by evaluating the entire design parameters with one flow field calculation.

1.3 Research questions

Based on the motivation and the approach from the previous section, the research questions are formulated:

- Can we identify the momentum forcing $\mathbf{f}$ necessary to reduce the base-model errors in specific test cases with data available?
- Can we identify Reynolds stress tensor components using only the mean DNS velocity vector field?

To provide answers to the formulated research questions, following tasks need to be achieved:

1. Formulate a deterministic optimization problem based on the Bayesian statistics.
2. Derive formulations for adjoint sensitivities and adjoint equations.
3. Validate adjoint sensitivities with finite-difference gradients.
4. Solve the deterministic optimization problem using the adjoint method.
5. Obtain the optimal estimate of the momentum forcing $\mathbf{f}$ through the optimization.
6. Extract the shear stress component from the optimal estimate of $\mathbf{f}$.

1.4 Outline

The thesis begins with introducing the base-model from the modification of the RANS momentum equation in Chapter 2. The detailed methodologies to perform the full-field inversion will be described in Chapter 3. Having obtained the optimal estimate of the momentum forcing $\mathbf{f}$ through the adjoint-based optimization, Chapter 4 will illustrate how to extract the shear stress components from the optimal estimate of $\mathbf{f}$. In Chapter 5, the implementation of the flow solvers as well as the optimization will be given. The test cases will be described in Chapter 6 and followed by the results and analysis in Chapter 7. The sensitivity validation is additionally performed in Chapter 8. Finally, Chapter 9 will present the conclusions and recommendations.

Chapter 2

RANS turbulence model vs Base-model

RANS simulations have been most widely used for the turbulence computation due to the lower computational cost compared to other approaches such as DNS and LES. The reduction in the computational cost is achieved by considering the time-averaged flow motion at one spatial location and velocity fluctuations separately (Leschziner, 2015). However, the velocity fluctuations introduce additional six unknowns to the momentum equation and the system become underdetermined. This issue is resolved by modelling the unknowns in terms of the eddy viscosity and the mean-strain-rate tensor. Nevertheless, the eddy viscosity modelling becomes a major part of which limits the accuracy of RANS turbulence predictions together with the classical calibration of closure coefficients. As an alternative of modelling the eddy viscosity, a base-model is considered. The base-model uses the momentum forcing vector field $\mathbf{f}$ to describes the turbulent force field. In later chapters, $\mathbf{f}$ will be inversely obtained by reducing the difference between the base-model and selected data. The aim of this chapter is to introduce the base-model with $\mathbf{f}$ and discuss its difference from the RANS turbulence model. Initially, RANS equations will be derived from Navier-Stokes equations. Then, a classical linear eddy viscosity model will be introduced and finally the base-model will be defined.

2.1 Reynolds-Averaged Navier-Stokes equations

The motion of an incompressible fluid is governed by conservation laws stating that mass and momentum of the fluid are conserved within the flow domain. The conservation laws can be described by the continuity equation and the Navier-Stokes momentum equation:

$$-\rho\nabla\cdot\mathbf{u} = 0 \tag{2.1}$$

$$\rho\frac{\partial\mathbf{u}}{\partial t} + \rho\nabla\cdot(\mathbf{u}\mathbf{u}) + \nabla p - \nabla\cdot(\mu(\nabla\mathbf{u} + (\nabla\mathbf{u})^T)) = 0 \tag{2.2}$$

where μ is the dynamic viscosity and ρ is the constant mass density. With initial and boundary conditions, the DNS computes the turbulent flow quantities $\mathbf{u}$ and p by solving (2.1) and (2.2), but requiring the high computational cost. To resolve this issue, the time-averaged flow quantities are considered in RANS simulations. The time-averaging approach gives the mean of the turbulent flow quantities over a time interval Δt at one spatial location (Moukalled et al., 2015). The expression of the mean value can be given by

$$\bar{\mathbf{u}}(t) = \frac{1}{\Delta t}\int_t^{t+\Delta t} \mathbf{u}(\tau)\, d\tau, \qquad \bar{p}(t) = \frac{1}{\Delta t}\int_t^{t+\Delta t} p(\tau)\, d\tau. \tag{2.3}$$

Based on the time-averaged flow quantities, an approach of decomposing the turbulent flow quantities in terms of their mean and fluctuations was introduced by Osborne Reynolds in 1985 (Launder, 2015). This is known as the Reynolds decomposition and is given by

$$\mathbf{u}(t) = \bar{\mathbf{u}}(t) + \mathbf{u}'(t), \qquad p(t) = \bar{p}(t) + p'(t) \tag{2.4}$$

where $\mathbf{u}'$ and p' correspond to the fluctuating components. The turbulence strength can be described as root-mean-square of the velocity fluctuations in Figure 2.1.

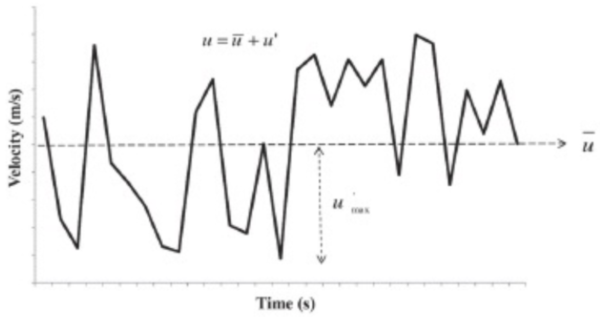

Figure 2.1: Velocity components of turbulent flow reproduced from Duarte et al. (2012)

The notations for velocity vector fields in this thesis are given by

$$\mathbf{u} = (u, v, w), \qquad \bar{\mathbf{u}} = (\bar{u}, \bar{v}, \bar{w}), \qquad \mathbf{u}' = (u', v', w') \tag{2.5}$$

and some useful time averaging rules can be introduced by

$$\begin{aligned} \overline{\mathbf{u}'} &= 0 \\ \bar{\bar{\mathbf{u}}} &= \bar{\mathbf{u}} \\ \overline{\nabla \bar{\mathbf{u}}} &= \nabla \bar{\mathbf{u}} \\ \overline{\bar{\mathbf{u}} + \mathbf{u}'} &= \bar{\mathbf{u}} \\ \overline{\frac{\partial(\bar{\mathbf{u}} + \mathbf{u}')}{\partial t}} &= \frac{\partial \bar{\mathbf{u}}}{\partial t} \\ \overline{(\bar{\mathbf{u}} + \mathbf{u}')(\bar{\mathbf{u}} + \mathbf{u}')} &= \bar{\mathbf{u}}\bar{\mathbf{u}} + \overline{\mathbf{u}'\mathbf{u}'}. \end{aligned} \tag{2.6}$$

Substituting the decomposed velocity and pressure from (2.4) to the incompressible Navier-Stokes equation (2.2) results in

$$\rho\frac{\partial(\bar{\mathbf{u}}+\mathbf{u}')}{\partial t}+\rho\nabla\cdot((\bar{\mathbf{u}}+\mathbf{u}')(\bar{\mathbf{u}}+\mathbf{u}'))+\nabla(\bar{p}+p') \\ -\nabla\cdot(\mu(\nabla(\bar{\mathbf{u}}+\mathbf{u}')+(\nabla(\bar{\mathbf{u}}+\mathbf{u}'))^T)) \quad =0. \tag{2.7}$$

Applying the time-averaging to (2.7) yields

$$\rho\frac{\partial(\overline{\bar{\mathbf{u}}+\mathbf{u}'})}{\partial t}+\rho\nabla\cdot(\overline{(\bar{\mathbf{u}}+\mathbf{u}')(\bar{\mathbf{u}}+\mathbf{u}')})+\nabla(\overline{\bar{p}+p'}) \\ -\nabla\cdot(\mu(\overline{\nabla(\bar{\mathbf{u}}+\mathbf{u}')+(\nabla(\bar{\mathbf{u}}+\mathbf{u}'))^T})) \quad =0. \tag{2.8}$$

Similarly, the substitution and time-averaging apply to the continuity equation (2.1), and it becomes

$$-\rho\nabla\cdot(\overline{\bar{\mathbf{u}}+\mathbf{u}'})=0. \tag{2.9}$$

Rearranging (2.8)and (2.9) based on (2.6) results

$$\rho\frac{\partial\bar{\mathbf{u}}}{\partial t}+\rho\nabla\cdot(\bar{\mathbf{u}}\bar{\mathbf{u}})+\nabla\bar{p}-\nabla\cdot(\mu D(\bar{\mathbf{u}})-\rho\overline{\mathbf{u}'\mathbf{u}'})=0 \tag{2.10}$$

$$-\rho\nabla\cdot\bar{\mathbf{u}}=0 \tag{2.11}$$

with the mean-strain-rate tensor

$$D(\bar{\mathbf{u}})=\frac{1}{2}(\nabla\bar{\mathbf{u}}+(\nabla\bar{\mathbf{u}})^T). \tag{2.12}$$

The above equations are knowns as the incompressible Reynolds-averaged Navier-Stokes (RANS) equations. In contrast to (2.1) and (2.2), they rely on the mean-flow quantities and their time-averaged fluctuations. The fluid is assumed to be a Newtonian fluid where the viscous stresses are generated from the flow and the viscous stress is linearly proportional to the strain-rate-tensor (Panton, 2013). This indicates that the time-averaged fluctuations are in a form of the stress tensor together with $\mu D(\bar{\mathbf{u}})$ in (2.10). The tensor representing the time-averaged velocity fluctuations is known as the Reynolds stress tensor and introduces six additional unknowns to the RANS momentum equation. The Reynolds stress tensor is a symmetric second-order tensor and is given by

$$\tau_{\mathbf{R}}=-\rho\overline{\mathbf{u}'\mathbf{u}'}=-\rho\begin{bmatrix}\overline{u'u'} & \overline{u'v'} & \overline{u'w'}\\ \overline{u'v'} & \overline{v'v'} & \overline{v'w'}\\ \overline{u'w'} & \overline{v'w'} & \overline{w'w'}\end{bmatrix} \tag{2.13}$$

where the diagonal components $\overline{u'u'}$, $\overline{v'v'}$ and $\overline{w'w'}$ represent normal stresses, and the remainders correspond to the shear stress components. These six additional unknowns in the Reynolds stress tensor make the system of the RANS equations underdetermined.

2.2 Linear eddy viscosity model

The underdetermined system due to the Reynolds averaging can be solved by modelling the Reynolds stress tensor. Based on the content from Moukalled et al. (2015), the Reynolds stress tensor can be modelled based on the Boussinesq hypothesis, which assumes that the Reynolds stress tensor is linearly proportional to the mean strain rate tensor such that

$$\tau_{\mathbf{R}} = -\rho\overline{\mathbf{u}'\mathbf{u}'} = 2\mu_t D(\bar{\mathbf{u}}) - \frac{2}{3}(\rho k + \mu_t(\nabla \cdot \bar{\mathbf{u}}))\mathbf{I} \tag{2.14}$$

where μ_t is the turbulent eddy viscosity, $\mathbf{I}$ is the Kronecker delta tensor and the turbulent kinetic energy k is defined as

$$k = \frac{1}{2}\mathbf{tr}(\overline{\mathbf{u}'\mathbf{u}'}). \tag{2.15}$$

The divergence of the flow velocity becomes zero due to the application of the incompressibility condition and (2.14) becomes

$$\tau_{\mathbf{R}} = -\rho\overline{\mathbf{u}'\mathbf{u}'} = \mu_t D(\bar{\mathbf{u}}) - \frac{2}{3}\rho k\mathbf{I}. \tag{2.16}$$

Substituting the approximated Reynolds tress tensor (2.16) into the RANS momentum equation (2.10) results in

$$\rho\frac{\partial\bar{\mathbf{u}}}{\partial t} + \rho\nabla\cdot(\bar{\mathbf{u}}\bar{\mathbf{u}}) + \nabla\bar{p} - \nabla\cdot(\mu D(\bar{\mathbf{u}}) + \mu_t D(\bar{\mathbf{u}}) - \frac{2}{3}\rho k\mathbf{I}) = 0. \tag{2.17}$$

Combining $\nabla \cdot \left(\frac{2}{3}\rho k\mathbf{I}\right)$ with the pressure gradient yields

$$\rho\frac{\partial\bar{\mathbf{u}}}{\partial t} + \rho\nabla\cdot(\bar{\mathbf{u}}\bar{\mathbf{u}}) + \nabla(\bar{p} + \frac{2}{3}\rho k) - \nabla\cdot((\mu + \mu_t)D(\bar{\mathbf{u}})) = 0. \tag{2.18}$$

The modified pressure can be re-defined as

$$\bar{p} \approx \bar{p} + \frac{2}{3}\rho k \tag{2.19}$$

and the final form of the RANS momentum equation with the linear approximation becomes

$$\rho\frac{\partial\bar{\mathbf{u}}}{\partial t} + \rho\nabla\cdot(\bar{\mathbf{u}}\bar{\mathbf{u}}) + \nabla\bar{p} - \nabla\cdot((\mu + \mu_t)D(\bar{\mathbf{u}})) = 0 \tag{2.20}$$

where the conservation of momentum is expressed by only two unknowns ($\bar{\mathbf{u}}$ and $\nabla\bar{p}$). Several turbulence models based on the Boussinesq hypothesis have been developed to approximate the eddy viscosity μ_t. Two-equation models have been the most widely used in industrial applications among other models such as algebraic, one-equation and second-order closure models. This is because solving two transport equations provides acceptable solution accuracy and requires relatively low computational costs compared to second-order closure models. As one of classical two-equation low-$\mathcal{R}e$ turbulence models, Launder-Sharma $k - \epsilon$ (Launder and Sharma, 1974) is considered in this chapter. The turbulence kinetic energy k and its dissipation rate ϵ are evaluated from its transport equations, which are given by

$$\frac{\partial(\rho k)}{\partial t} + \nabla \cdot \left(\rho k \bar{\mathbf{u}} - \left(\mu + \frac{\mu_t}{\sigma_k} \right) \nabla k \right) = P - \rho\epsilon - D \tag{2.21}$$

$$\frac{\partial(\rho \epsilon)}{\partial t} + \nabla \cdot \left(\rho \epsilon \bar{\mathbf{u}} - \left(\mu + \frac{\mu_t}{\sigma_\epsilon} \right) \nabla \epsilon \right) = (C_1 P - C_2 \rho\epsilon)\frac{\epsilon}{k} + E \tag{2.22}$$

with the eddy viscosity μ_t and th turbulence production P

$$\mu_t = C_\mu \rho \frac{k^2}{\epsilon}, \qquad P = \tau_{\mathbf{R}} \nabla(\bar{\mathbf{u}}^T) \tag{2.23}$$

where

$$C_\mu = 0.09 \left[\exp\left(\frac{-3.4}{(1 + \frac{\mathcal{R}e_T}{50})^2} \right) \right], \qquad C_2 = 1.92 \left[1.0 - 0.3 \exp(-\mathcal{R}e_T^2) \right], \tag{2.24}$$

$$C_1 = 1.44, \qquad \sigma_k = 1, \qquad \sigma_\epsilon = 1.3 \tag{2.25}$$

and

$$\mathcal{R}e_T = \frac{\rho k^2}{\mu \epsilon}. \tag{2.26}$$

The extra source terms D and E are given by

$$D = 2\mu \left(\nabla(\sqrt{k}) \right)^2, \qquad E = 2\frac{\mu\mu_t}{\rho} \left(\nabla^2(\bar{\mathbf{u}}^T) \right)^2 \tag{2.27}$$

and they become active when evaluating k and ϵ within the viscous sublayer. The viscous sublayer is the region close to wall boundaries where the turbulent flow become laminar due to no-slip boundary conditions (Iaccarino, 2004). In this region, the transport process is dominated by molecular viscous effects, thus applying the extra source terms as the special wall treatment. Applying the no-slip boundary conditions also implies

$$k_{wall} = 0. \tag{2.28}$$

Substituting (2.28) into (2.21) gives

$$\epsilon_{wall} = -D = -2\mu \left(\nabla(\sqrt{k_{wall}}) \right)^2 = 0. \tag{2.29}$$

2.3 Base-model

In the previous section, the eddy viscosity μ_t is modelled based on k and ϵ. Together with the mean-strain-rate tensor, μ_t represents the approximated behaviour of the velocity fluctuations. Alternatively, in this section, the divergence of the Reynolds stress tensor is fully replaced by the momentum forcing $\mathbf{f}$ such that

$$\nabla \cdot \rho\overline{\mathbf{u'u'}} = \mathbf{f}. \tag{2.30}$$

The RANS momentum equation (2.10) is modified by (2.30). Together with the continuity equation, base-model equations can be formulated by

$$\mathcal{R}_1 = \rho\nabla \cdot (\bar{\mathbf{u}}\bar{\mathbf{u}}) + \nabla\bar{p} - \nabla \cdot (2\mu D(\bar{\mathbf{u}})) + \mathbf{f} = 0 \tag{2.31}$$
$$\mathcal{R}_2 = -\rho\nabla \cdot \bar{\mathbf{u}} = 0 \tag{2.32}$$

where $\mathcal{R}_i$ is the residual representation of the base-model equations. While the RANS model computes the eddy viscosity μ_t to predict the flow field by solving the transport equations (2.21) and (2.21), the base-model predicts the flow field by obtaining $\mathbf{f}$ through the full-field inversion technique. In addition, various modifications can be made on the base-model momentum equation. For example, if a choice of the momentum force is made by

$$\mathbf{f} = -\mu_t D(\bar{\mathbf{u}}), \tag{2.33}$$

then the base-model will produce the exactly same flow field as the RANS prediction. When zero momentum force is applied such that

$$\mathbf{f} = 0, \tag{2.34}$$

then the base-model will simulate the behaviour of the RANS prediction with $\mu_t = 0$, which is basically a laminar flow field. At the wall boundaries, no-slip conditions are applied, thus no momentum forcing $\mathbf{f}$.

Chapter 3

Full-Field Inversion

In Section 2.3, the momentum forcing $\mathbf{f}$ is introduced to represent the divergence of the Reynolds stress tensor in the base-model momentum equation (2.31). As previously discussed, the choice of $\mathbf{f}$ has the significant influence on the base-model predictions. The full-field inversion technique will be used to determine the optimal choice for $\mathbf{f}$ in this work.

Parish and Duraisamy (2015) initially apply the full-field inversion technique to quantify the RANS model-form errors. The main idea of their approach is to estimate the functional errors and correct the turbulence production based on the estimated errors by performing the full-field inversion. The main drawback of their approach is that it still relies on the Boussinesq approximation and will not give any improvement for flows in which the turbulent anisotropy plays a role, e.g. duct flows or any other flow cases with secondary circulations.

To compensate the drawback of Parish and Duraisamy (2015)'s approach, this thesis avoids the Boussinesq approximation by replacing the divergence of the Reynolds stress tensor with the momentum forcing $\mathbf{f}$ and applies the full-field inversion for correcting the momentum forcing $\mathbf{f}$ to reduce the base-model errors.

In the following sections, the methodology of the full-field inversion will be illustrated. To begin with, this chapter will state a linear problem to be solved. Then the problem will be transformed into a deterministic optimization problem by reducing the complexity of the Bayesian framework. As gradient-based optimization is used to solve the deterministic problem in this work, two different optimization algorithms will be discussed. A choice of the gradient computation will be made between the finite difference approximation and the continuous adjoint method. Finally, continuous adjoint equations will be derived in regard to the base-model.

3.1 Problem statement

The base-model operator is defined as $\mathbf{H}(\cdot)$. When the base-model produces the same flow field as the dataset $\mathbf{d}$ by imposing the momentum forcing $\mathbf{f}$, a linear system can be constructed such that

$$\mathbf{d} = \mathbf{H}(\mathbf{f}). \tag{3.1}$$

If the system is discrete-linear, (3.1) can be written as

$$\mathbf{d} = \mathbf{H}\mathbf{f} \tag{3.2}$$

where $\mathbf{H}$ is an operator matrix. If $\mathbf{H}$ is an invertible-square matrix, the system (3.2) can be solved by multiplying the inverse of $\mathbf{H}$ to the both sides of (3.2). Thus, $\mathbf{f}$ can be obtained by

$$\mathbf{f} = \mathbf{H}^{-1}\mathbf{d}. \tag{3.3}$$

However, Wunsch (1997) states that the operator matrix is not always invertible especially when there exists little information to determine an unique solution for a given system. The base-model does not have the capability of evaluating $\mathbf{f}$ satisfying the dataset $\mathbf{d}$. This implies that $\mathbf{H}$ is no longer invertible. Hence, the problem needs to be solved by an inverse approach. With the given dataset $\mathbf{d}$, the optimal value of $\mathbf{f}$ can be estimated by performing optimization. The idea of the optimization is to obtain the optimal estimate $\mathbf{f}^*$ for the momentum forcing $\mathbf{f}$ by minimizing the gap between the dataset $\mathbf{d}$ and the base-model $\mathbf{H}(\mathbf{f})$ such that

$$\underset{\mathbf{f}}{\text{minimize}}\, |\mathbf{d} - \mathbf{H}(\mathbf{f})| \,. \tag{3.4}$$

During the optimization, $\mathbf{f}$ is considered as a design variable and contains the equal number of dimension as the flow velocity field. Evaluating $\mathbf{f}_i$ at a particular point i requires one flow calculation. As a consequence, the optimization may lead to the drastic increase in the number of the flow calculations and result in requiring a high computation cost. To resolve the issue, the inverse problem is solved using the adjoint optimization. The continuous adjoint approach (Othmer, 2008) is used in this work and the detail will be provided in later sections.

3.2 Deterministic optimization problem

High-fidelity results such as DNS and experimental measurements may contain stochastic behaviour of turbulent flows. On the other hand, the base-model in this work is limited to generate the stochastic feature of the turbulence. When the dataset $\mathbf{d}$ is to be such high-fidelity results, it is expected to observe some statistical errors in the base-model. Since the thesis aims to obtain the deterministic solution for the momentum forcing $\mathbf{f}$, it is required to construct the deterministic optimization problem. Based on the work of Parish and Duraisamy (2016), the deterministic optimization problem will be formulated in this section. Initially, the posterior of $\mathbf{f}$ can be expressed based on the data $\mathbf{d}$ as

$$\mathbf{p}(\mathbf{f}|\mathbf{d}) = \frac{\mathbf{p}(\mathbf{d}|\mathbf{f})\mathbf{p}_o(\mathbf{f})}{\mathbf{p}(\mathbf{d})} \tag{3.5}$$

where $\mathbf{p}(\mathbf{d}|\mathbf{f})$ is the likelihood and $\mathbf{p}_o(\mathbf{f})$ is the prior. Since $\mathbf{p}(\mathbf{d})$ is independent of $\mathbf{f}$, the posterior distribution is proportional to the likelihood times prior shown as

$$\mathbf{p}(\mathbf{f}|\mathbf{d}) \propto \mathbf{p}(\mathbf{d}|\mathbf{f})\mathbf{p}_o(\mathbf{f}) \tag{3.6}$$

The likelihood $\mathbf{p}(\mathbf{d}|\mathbf{f})$ is based on the dataset $\mathbf{d}$ which is statistically modelled by

$$\mathbf{d} = \mathbf{H}(\mathbf{f}) + \boldsymbol{\epsilon}_s \tag{3.7}$$

where the base-model uncertainty ϵ_s is assumed to be Gaussian such that

$$\boldsymbol{\epsilon}_s \sim \mathcal{N}(0, \mathbf{C}_\mathbf{d}) \tag{3.8}$$

with the observational covariance matrix $\mathbf{C}_\mathbf{d}$. This allows us to assume that the difference between the dataset $\mathbf{d}$ and the base-model $\mathbf{H}(\mathbf{f})$ is also Gaussian. Subsequently, the likelihood can be written as

$$\mathbf{p}(\mathbf{d}|\mathbf{f}) = \frac{1}{\sqrt{(2\pi)^n \det(\mathbf{C}_\mathbf{d})}} \exp\left(-\frac{1}{2}\left(\mathbf{d} - \mathbf{H}(\mathbf{f})\right)^T {\mathbf{C}_\mathbf{d}}^{-1}\left(\mathbf{d} - \mathbf{H}(\mathbf{f})\right)\right) \tag{3.9}$$

where n is the number of discretization points. Applying the same Gaussian assumption to $\mathbf{f}$ with the expected prior $\mathbf{f}_{prior}$ gives

$$\mathbf{p}(\mathbf{f}) = \frac{1}{\sqrt{(2\pi)^n \det(\mathbf{C}_\mathbf{f})}} \exp\left(-\frac{1}{2}\left(\mathbf{f} - \mathbf{f}_{prior}\right)^T {\mathbf{C}_\mathbf{f}}^{-1}\left(\mathbf{f} - \mathbf{f}_{prior}\right)\right) \tag{3.10}$$

where $\mathbf{C}_\mathbf{f}$ is the prior covariance matrix. With (3.9) and (3.10), the posterior (3.6) becomes

$$\mathbf{p}(\mathbf{f}|\mathbf{d}) \propto \exp\left[-\frac{1}{2}\left(\left(\mathbf{d} - \mathbf{H}(\mathbf{f})\right)^T {\mathbf{C}_\mathbf{d}}^{-1}\left(\mathbf{d} - \mathbf{H}(\mathbf{f})\right) + \left(\mathbf{f} - \mathbf{f}_{prior}\right)^T {\mathbf{C}_\mathbf{f}}^{-1}\left(\mathbf{f} - \mathbf{f}_{prior}\right)\right)\right] \tag{3.11}$$

The maximum a posteriori (MAP) (Tarantola, 2005) for $\mathbf{f}$ can be obtained when the negative of the exponent in (3.11) is minimum. The expression for the MAP estimate $\mathbf{f}^*$ is given by

$$\mathbf{f}^* \simeq \arg\min_{\mathbf{f}} \frac{1}{2}\left[\left(\mathbf{d} - \mathbf{H}(\mathbf{f})\right)^T {\mathbf{C}_\mathbf{d}}^{-1}\left(\mathbf{d} - \mathbf{H}(\mathbf{f})\right) + \left(\mathbf{f} - \mathbf{f}_{prior}\right)^T {\mathbf{C}_\mathbf{f}}^{-1}\left(\mathbf{f} - \mathbf{f}_{prior}\right)\right]. \tag{3.12}$$

Diagonal covariance matrices for $\mathbf{C_d}$ and $\mathbf{C_f}$ are considered in this framework. This assumes that both data are uncorrelated with the results of each base-model quantity. Furthermore, if $\mathbf{C_f}$ is assumed to be much higher than $\mathbf{C_d}$, the deterministic problem (3.12) can be further simplified such that

$$\mathbf{f}^* \simeq \arg\min_{\mathbf{f}} \frac{1}{2}\left[(\mathbf{d}-\mathbf{H}(\mathbf{f}))^T \mathbf{C_d}^{-1} (\mathbf{d}-\mathbf{H}(\mathbf{f}))\right]. \tag{3.13}$$

This is basically a least squares cost function, which is based on a diagonal covariance matrix $\mathbf{C_d}$ and no prior. With a integral form of the cost function (3.13) for the entire flow domain, the deterministic optimization problem constrained by (2.31) and (2.32) can be formulated by

$$\mathbf{f}^* \simeq \arg\min_{\mathbf{f}} J(\bar{\mathbf{u}}) \qquad \text{subject to} \qquad \mathcal{R}(\mathbf{f}, \bar{\mathbf{u}}) = 0 \ \text{ on } (\Omega, \Gamma) \tag{3.14}$$

with

$$\mathcal{R} = (\mathcal{R}_1, \mathcal{R}_2)^T \tag{3.15}$$

and

$$J(\bar{\mathbf{u}}) = \int_\Omega J_\Omega \, d\Omega + \int_\Gamma J_\Gamma \, d\Gamma \tag{3.16}$$

$$= \int_\Omega \frac{\sigma}{2}(\bar{\mathbf{u}}_\mathbf{d} - \bar{\mathbf{u}})^2 \, d\Omega + \int_\Gamma \frac{\sigma}{2}(\bar{\mathbf{u}}_\mathbf{d} - \bar{\mathbf{u}})^2 \, d\Gamma. \tag{3.17}$$

where Ω and Γ are the interior and boundary domains respectively. σ is the scalar representation of the diagonal component of $\mathbf{C_d}$. The cost function J is constructed to minimize the difference in the velocity fields. The choice of σ will be discussed when results are presented.

3.3 Gradient-based optimization

A gradient-based optimization is considered in order to minimize the cost function (3.13) in this framework. The gradient-based method iteratively searches for a minimum of the cost function with the directions based on its gradient (Nocedal and Wright, 2006). The general algorithm of the gradient-based method can be described as following steps.

1. Convergence test.
2. A search direction computation.
3. A step length computation.
4. Update of the design variable $\mathbf{f}_{k+1}$.

The design variable $\mathbf{f}_{k+1}$ is updated based on the previous optimal guess $\mathbf{f}_k$, the search direction p_k and the step length α_k as

$$\mathbf{f}_{k+1} = \mathbf{f}_k + \alpha_k p_k \tag{3.18}$$

with the condition of the step length to be a positive scalar such that

$$J(\mathbf{f}_k + \alpha_k p_k) < J(\mathbf{f}_k) \tag{3.19}$$

where $J(\mathbf{f})$ is the function to be minimized. There exist various types of gradient-based optimization algorithms depending on the method that is used to determine the search direction p_k. Based on contents of Hicken et al. (2012) and Nocedal and Wright (2006), the theory of steepest-descent and quasi-Newton methods will be discussed in following subsections.

3.3.1 Steepest-descent method

Steepest-descent uses the gradient vector as the search direction. The first-order gradient G_k for the function $J(\mathbf{f})$ can be simply obtained by the first-order Taylor-series expansion

$$J(\mathbf{f}_k + s_k) = J(\mathbf{f}_k) + G_k^T s_k + \mathcal{O}(s_k^2) \tag{3.20}$$

where s_k is the step. Taking a derivative with respect to s_k results in

$$G_k = J'(\mathbf{f}_k) \tag{3.21}$$

Steepest-descent finds the minimum of the cost function in the search direction. The search direction is the negative-normalized gradient, i.e.

$$p_k = -\frac{G_k}{\|G_k\|}. \tag{3.22}$$

Substituting the search direction (3.22) into the equation (3.18) gives the current location update formulation (3.23) for the steepest descent algorithm:

$$\mathbf{f}_{k+1} = \mathbf{f}_k - \alpha_k \frac{G_k}{\|G_k\|} \tag{3.23}$$

where the step length α_k is determined by line search. The iteration continues until the chosen convergence criteria is satisfied. Although the steepest descent method is easy to implement, it is known to be an inefficient method particularly when the solution approaches more to the minimum of the cost function due to its zigzags characteristic shown in Figure 3.1. Beside, since the proper step length is not always evaluated in this algorithm, it requires the additional information to determine the step length (Nocedal and Wright, 2006).

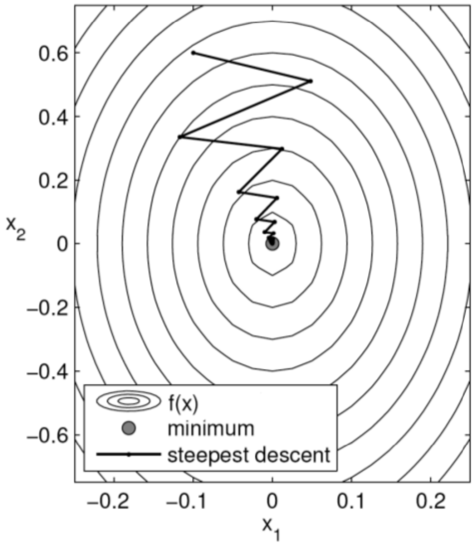

Figure 3.1: Solution history of steepest-descent reproduced from Hicken et al. (2012)

3.3.2 Quasi-Newton method

The quasi-Newton method use a Hessian approximation of $\nabla^2_{\mathbf{f}} J$ for the search direction p_k. The explanation about the quasi-Newton algorithm can be begun from the Newton method, which uses a second order Taylor series expansion for the function $J(\mathbf{f})$:

$$J(\mathbf{f}_k + s_k) \approx J(\mathbf{f}_k) + G_k^T s_k + \frac{1}{2} s_k^T H_k s_k \tag{3.24}$$

where $H(\mathbf{f}_k)$ is the Hessian. Setting the derivative of (3.24) with respect to s_k to be zero leads to

$$s_k = -H_k^{-1} G_k \tag{3.25}$$

Using (3.18), an updated formulation of the current position for the Newton method becomes

$$\mathbf{f}_{k+1} = \mathbf{f}_k - H_k^{-1} G_k. \tag{3.26}$$

The Newton method requires to compute the Hessian as well as the gradient in order to determine the search direction p_k. The computation of the Hessian requires a high number of second-order derivatives. Instead of computing the full Hessian, the quasi-Newton algorithm uses a Hessian approximation. There are various methods to approximate the Hessian. One of the most well known methods is the Broyden Fletcher Goldfarb Shanno (BFGS) algorithm:

$$H_{k+1}^{-1} = \left(I - \frac{s_k y_k^T}{s_k^T y_k} \right) H_k^{-1} \left(I - \frac{s_k y_k^T}{s_k^T y_k} \right) + \frac{s_k s_k^T}{s_k^t y_k} \tag{3.27}$$

with

$$y_k = G_{k+1} - G_k \tag{3.28}$$

where y_k is defined as the variance of the gradient and I is the identity matrix. Figure 3.2 shows an example of the solution path of the BFGS quasi-Newton method. Compared to steepest-descent (3.1), less iterations are required to reach the minimum of the cost function and it is known to be the most effective method even among other quasi-Newton algorithms (Hicken et al., 2012).

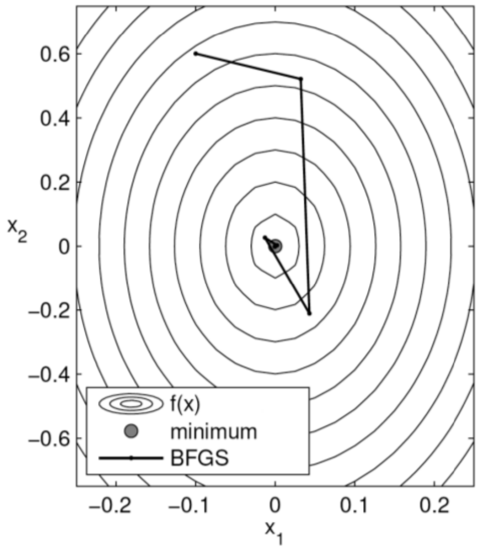

Figure 3.2: Solution history of BFGS quasi-Newton reproduced from Hicken et al. (2012)

3.4 Gradient computation

Gradient-based optimization methods require the derivative computation of the cost function with respect to the design variable. The finite difference method provides a generic way to compute the gradients. However, the number of gradient evaluations proportionally increases with the number of design parameters. Alternatively, the gradients can be efficiently computed by using the continuous adjoint approach. Both approaches will be discussed together with their use in this section.

3.4.1 Finite difference method

The purpose of the finite difference is to validate the adjoint sensitivities in this work due to the large number of the design parameters. Following the work of LeVeque (2007), the standard definition of the derivative for the cost function J is given by

$$J'(\mathbf{f}) = \lim_{\Delta\mathbf{f}\to 0} \frac{J(\mathbf{f}+\Delta\mathbf{f}) - J(\mathbf{f})}{\Delta\mathbf{f}}. \tag{3.29}$$

The definition can be written in terms of discrete set of points $\mathbf{f}$ as

$$J'(\mathbf{f_k}) \approx \frac{J(\mathbf{f_k}+\Delta\mathbf{f_k}) - J(\mathbf{f_k})}{\Delta\mathbf{f_k}}. \tag{3.30}$$

The formulation (3.30) is known as a *forward Euler* approximation. Other equally valid approximations exist such as *backward Euler* and *central difference* based on the choice of offset. The *forward Euler* approximation is used in this work. By Taylor series expansion, the cost function J at $\mathbf{f_{k+1}}$ is expanded about $\mathbf{f_k}$ as

$$J(\mathbf{f_k}+\Delta\mathbf{f_k}) = J(\mathbf{f_k}) + \Delta\mathbf{f_k}\frac{\partial J}{\partial\mathbf{f}}\bigg|_{\mathbf{f_k}} + \frac{\Delta\mathbf{f_k}^2}{2}\frac{\partial^2 J}{\partial\mathbf{f}^2}\bigg|_{\mathbf{f_k}} + \frac{\Delta\mathbf{f_k}^3}{6}\frac{\partial^3 J}{\partial\mathbf{f}^3}\bigg|_{\mathbf{f_k}} + \cdots \tag{3.31}$$

Rearranging (3.31) gives

$$\frac{J(\mathbf{f_k}+\Delta\mathbf{f_k}) - J(\mathbf{f_k})}{\Delta\mathbf{f_k}} - \frac{\partial J}{\partial\mathbf{f}}\bigg|_{\mathbf{f_k}} = \frac{\Delta\mathbf{f_k}}{2}\frac{\partial^2 J}{\partial\mathbf{f}^2}\bigg|_{\mathbf{f_k}} + \frac{\Delta\mathbf{f_k}^2}{6}\frac{\partial^3 J}{\partial\mathbf{f}^3}\bigg|_{\mathbf{f_k}} + \cdots \tag{3.32}$$

The left hand side of (3.32) indicates the difference between the finite-difference derivative and the exact derivative. This difference is referred to as the truncation error, which is shown on the right hand side of (3.32). The truncation error depends on the higher order derivatives and the step size $\Delta\mathbf{f_k}$. Thus, the exact derivative of J at a particular design parameter $\mathbf{f_k}$ can be expressed as

$$\frac{\partial J}{\partial\mathbf{f}}\bigg|_{\mathbf{f_k}} = \frac{J(\mathbf{f_k}+\Delta\mathbf{f_k}) - J(\mathbf{f_k})}{\Delta\mathbf{f_k}} + O(\Delta\mathbf{f_k}) \tag{3.33}$$

where $O(\Delta\mathbf{f_k})$ indicates the truncation error. The total numerical errors for the finite-difference approximation consist of both the truncation and round-off errors. Figure 3.3 shows the behaviour of both errors over the step size. The truncation error increases with the step size whereas the round-off error decreases. This is because the step size is the multiplication factor in the truncation error expression and simultaneously the variance of the cost function J is divided by the step size. The point of diminishing returns in Figure 3.3 is the point where the total error is at minimum, and its corresponding x-axis is the step size to be chosen.

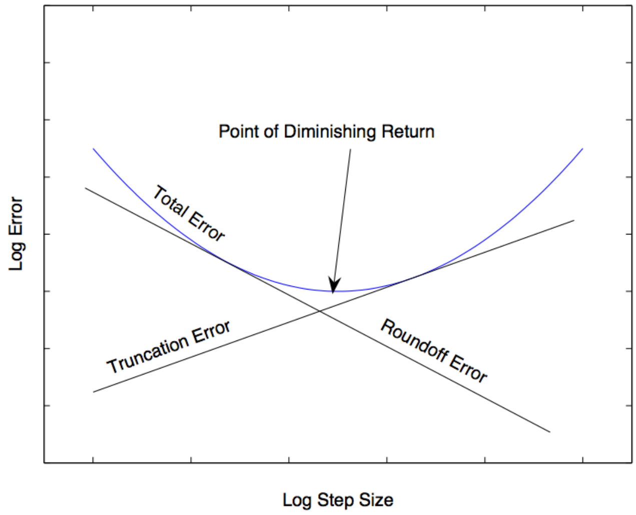

Figure 3.3: Round-off and truncation error behaviour reproduced from (Advanced Navigation and Control Systems Laboratory, 2012)

3.4.2 Continuous adjoint sensitivity

Large numbers of design parameters have encouraged the use of adjoint sensitivities in the optimizations involving CFD simulations. The high dimensionality issue of the design variable in optimization is problematic as it requires numbers of gradient evaluations. The adjoint method makes the gradient computation become the least dependent on the number of design parameters (Dwight and Brezillon, 2008). The adjoint method can be categorized into two different approaches: discrete adjoint and continuous adjoint. Nadarajah and Jameson (2001) discuss the difference between the two adjoint approaches. They state that the continuous adjoint method performs better in regards to the balance between accuracy and efficiency in interior domain while the discrete adjoint approach is more superior at boundary domain. The continuous adjoint approach is considered in this work. Firstly, sets of both primal and adjoint variables are defined by

$$\boldsymbol{\omega} = (\bar{\mathbf{u}}, \bar{p})^T, \qquad \boldsymbol{\psi} = (\mathbf{v}, q)^T \tag{3.34}$$

where $\boldsymbol{\omega}$ and $\boldsymbol{\psi}$ correspond to primal and adjoint notations respectively. Based on the work of Othmer (2008), *Lagrangian* $\mathcal{L}$ can be defined by introducing the adjoint variables $\boldsymbol{\psi}$ to governing equations such that

$$\mathcal{L} = J + \int_\Omega \boldsymbol{\psi} \cdot \mathcal{R} \, d\Omega. \tag{3.35}$$

Since the evaluation of the domain integration (3.35) equals to zero due to the residual term inside,

$$\mathcal{L} = J, \qquad \forall \boldsymbol{\psi} \tag{3.36}$$

The total variation of the *Lagrangian* cost function with respect to both $\mathbf{f}$ and $\boldsymbol{\omega}$ is given by

$$\delta\mathcal{L} = \frac{\partial \mathcal{L}}{\partial \mathbf{f}} \cdot \delta\mathbf{f} + \frac{\partial \mathcal{L}}{\partial \boldsymbol{\omega}} \cdot \delta\boldsymbol{\omega} = \delta_{\mathbf{f}}\mathcal{L} + \delta_{\boldsymbol{\omega}}\mathcal{L} \tag{3.37}$$

where δ is the variation operator. Applying the same variation operator to (3.35) yields

$$\delta\mathcal{L} = \delta J + \int_{\Omega} \boldsymbol{\psi} \cdot \delta\mathcal{R}\, d\Omega. \tag{3.38}$$

If the adjoint quantities $\boldsymbol{\psi}$ are selected such that

$$\delta_{\boldsymbol{\omega}}\mathcal{L} = 0, \tag{3.39}$$

the total variation 3.37 becomes

$$\delta\mathcal{L} = \delta_{\mathbf{f}}\mathcal{L}. \tag{3.40}$$

Expanding (3.38) further based on (3.40) gives

$$\delta\mathcal{L} = \delta_{\mathbf{f}}\mathcal{L} = \delta_{\mathbf{f}} J + \int_{\Omega} \boldsymbol{\psi} \cdot \delta_{\mathbf{f}}\mathcal{R}\, d\Omega. \tag{3.41}$$

Taking the derivative of 3.41 with respect to $\mathbf{f}$ results in the sensitivity expression:

$$\frac{\partial \mathcal{L}}{\partial \mathbf{f}} = \frac{\partial J}{\partial \mathbf{f}} + \int_{\Omega} \boldsymbol{\psi} \cdot \frac{\partial \mathcal{R}}{\partial \mathbf{f}}\, d\Omega \tag{3.42}$$

With the given cost function (3.16), the derivative of the cost function J with respect to $\mathbf{f}$ becomes

$$\frac{\partial J}{\partial \mathbf{f}} = 0. \tag{3.43}$$

The constrain $\mathcal{R}$ is defined as a set of the base-model equations (2.31) and (2.32). Taking the derivative of $\mathcal{R}$ with respect to $\mathbf{f}$ results

$$\frac{\partial \mathcal{R}}{\partial \mathbf{f}} = \left(\frac{\partial \mathcal{R}_1}{\partial \mathbf{f}}, \frac{\partial \mathcal{R}_2}{\partial \mathbf{f}} \right)^T. \tag{3.44}$$

Based on (3.43) and (3.44), the expression for the adjoint sensitivities can be given by

$$\frac{\partial \mathcal{L}}{\partial \mathbf{f}} = \int_{\Omega} \mathbf{v} \cdot \frac{\partial \mathcal{R}_1}{\partial \mathbf{f}} + q \frac{\partial \mathcal{R}_2}{\partial \mathbf{f}}\, d\Omega = \int_{\Omega} \mathbf{v}\, d\Omega = \mathbf{v} \cdot \boldsymbol{\Omega} \tag{3.45}$$

where the $\boldsymbol{\Omega}$ indicates the volume vector field of the given flow geometry. The adjoint sensitivities are used as search directions in the gradient-based optimization. While the finite difference gradients are determined based on the choice of the step size of which the total numerical error is at minimum, the adjoint sensitivity only involves cheap derivatives with respect to the design variable $\mathbf{f}$. Therefore, it is concluded that the adjoint sensitivities are preferred over the finite-different gradients in the high dimensional optimization problem.

3.5 Derivation of continuous adjoint equations

Appropriate derivations of the adjoint equations are fundamental basis of the adjoint framework as the adjoint variables are necessary to compute the adjoint sensitivities. This section will address full derivations of continuous adjoint formulations for the base-model equations (2.31) and (2.32). The derivation starts by choosing the adjoint variables $\boldsymbol{\psi}$ satisfying the condition (3.39) such that

$$\delta_{\boldsymbol{\omega}}\mathcal{L} = \delta_{\boldsymbol{\omega}}J + \int_\Omega \boldsymbol{\psi} \cdot \delta_{\boldsymbol{\omega}}\mathcal{R}\, d\Omega = 0. \tag{3.46}$$

The variation of (3.15) with respect to the primal variables $\boldsymbol{\omega}$ is expanded as

$$\begin{aligned} \delta_{\boldsymbol{\omega}}\mathcal{R} &= \delta_{\bar{\mathbf{u}}}\mathcal{R} + \delta_{\bar{p}}\mathcal{R} && (3.47)\\ &= \begin{pmatrix}\delta_{\bar{\mathbf{u}}}\mathcal{R}_1\\ \delta_{\bar{\mathbf{u}}}\mathcal{R}_2\end{pmatrix} + \begin{pmatrix}\delta_{\bar{p}}\mathcal{R}_1\\ \delta_{\bar{p}}\mathcal{R}_2\end{pmatrix} && (3.48)\end{aligned}$$

with

$$\delta_{\bar{\mathbf{u}}}\mathcal{R}_1 = \frac{\partial \mathcal{R}_1}{\partial \bar{\mathbf{u}}}\delta\bar{\mathbf{u}} = \rho(\delta\bar{\mathbf{u}}\cdot\nabla)\bar{\mathbf{u}} + \rho(\bar{\mathbf{u}}\cdot\nabla)\delta\bar{\mathbf{u}} - \nabla\cdot(2\mu D(\delta\bar{\mathbf{u}})), \tag{3.49}$$

$$\delta_{\bar{\mathbf{u}}}\mathcal{R}_2 = \frac{\partial \mathcal{R}_2}{\partial \bar{\mathbf{u}}}\delta\bar{\mathbf{u}} = -\rho\nabla\cdot\delta\bar{\mathbf{u}}, \tag{3.50}$$

$$\delta_{\bar{p}}\mathcal{R}_2 = \frac{\partial \mathcal{R}_2}{\partial \bar{p}}\delta\bar{p} = \nabla\delta\bar{p}, \tag{3.51}$$

$$\delta_{\bar{p}}\mathcal{R}_2 = \frac{\partial \mathcal{R}_2}{\partial \bar{p}}\delta\bar{p} = 0. \tag{3.52}$$

Applying the variation operator with respect to the flow variables to the cost function (3.16) gives

$$\begin{aligned} \delta_{\boldsymbol{\omega}}J &= \int_\Omega \frac{\partial J_\Omega}{\partial \boldsymbol{\omega}}\delta\boldsymbol{\omega}\, d\Omega + \int_\Gamma \frac{\partial J_\Gamma}{\partial \boldsymbol{\omega}}\delta\boldsymbol{\omega}\, d\Gamma && (3.53)\\ &= \int_\Omega \frac{\partial J_\Omega}{\partial \bar{\mathbf{u}}}\delta\bar{\mathbf{u}}\, d\Omega + \int_\Gamma \frac{\partial J_\Gamma}{\partial \bar{\mathbf{u}}}\delta\bar{\mathbf{u}}\, d\Gamma + \int_\Omega \frac{\partial J_\Omega}{\partial \bar{p}}\delta\bar{p}\, d\Omega + \int_\Gamma \frac{\partial J_\Gamma}{\partial \bar{p}}\delta\bar{p}\, d\Gamma && (3.54)\\ &= \int_\Omega \sigma(\bar{\mathbf{u}} - \bar{\mathbf{u}}_{\mathbf{d}})\delta\bar{\mathbf{u}}\, d\Omega + \int_\Gamma \sigma(\bar{\mathbf{u}} - \bar{\mathbf{u}}_{\mathbf{d}})\delta\bar{\mathbf{u}}\, d\Gamma. && (3.55)\end{aligned}$$

The resulted $\delta_{\boldsymbol{\omega}}J$ indicates that the derivatives respect to the pressure variable disappear as the cost function J is only dependent on the primal velocity variable. Substituting 3.48 and 3.55 into 3.46 yields

$$\begin{aligned} \delta_{\boldsymbol{\omega}}\mathcal{L} &= 0 && (3.56)\\ &= \int_\Omega \sigma(\bar{\mathbf{u}} - \bar{\mathbf{u}}_{\mathbf{d}})\delta\bar{\mathbf{u}}\, d\Omega + \int_\Gamma \sigma(\bar{\mathbf{u}} - \bar{\mathbf{u}}_{\mathbf{d}})\delta\bar{\mathbf{u}}\, d\Gamma \\ &\quad + \int_\Omega \begin{pmatrix}\mathbf{v}\\ q\end{pmatrix} \cdot \begin{pmatrix}\rho(\delta\bar{\mathbf{u}}\cdot\nabla)\bar{\mathbf{u}} + \rho(\bar{\mathbf{u}}\cdot\nabla)\delta\bar{\mathbf{u}} - \nabla\cdot(2\mu D(\delta\bar{\mathbf{u}})) + \nabla\delta\bar{p}\\ -\rho\nabla\cdot\delta\bar{\mathbf{u}}\end{pmatrix} d\Omega. && (3.57)\end{aligned}$$

For any arbitrary value of $\delta\bar{\mathbf{u}}$ and $\delta\bar{p}$, the condition defined in (3.56) should still hold. In order to always satisfy the condition, it is necessary to separate both $\delta\bar{\mathbf{u}}$ and $\delta\bar{p}$ from other terms regarding (3.57). For this purpose, the integration by parts is a key technique. Hinterberger and Olesen (2011) provides specific rules for the partial integration that is applicable for this case and they are given by

$$\int_\Omega s(\nabla\cdot\mathbf{F})\,d\Omega = \int_\Omega \nabla\cdot(s\mathbf{F})\,d\Omega - \int_\Omega \mathbf{F}\cdot\nabla s\,d\Omega \tag{3.58}$$

and

$$\int_\Omega \mathbf{F}\cdot(\nabla s)\,d\Omega = \int_\Omega \nabla\cdot(\mathbf{F}s)\,d\Omega - \int_\Omega s\nabla\cdot\mathbf{F}\,d\Omega \tag{3.59}$$

where s represents the scalar field while $\mathbf{F}$ is denoted by the vector field. By the divergence theorem, the volume integration of the divergence of the vector field can be replaced by the surface integral

$$\int_\Omega \nabla\cdot(s\mathbf{F})\,d\Omega = \int_\Gamma \mathbf{F}\cdot s\mathbf{n}\,d\Gamma \tag{3.60}$$

and

$$\int_\Omega \nabla\cdot(\mathbf{F}s)\,d\Omega = \int_\Gamma s\mathbf{F}\cdot\mathbf{n}\,d\Gamma. \tag{3.61}$$

Substituting 3.60 and 3.61 into 3.58 and 3.59 respectively gives

$$\int_\Omega s(\nabla\cdot\mathbf{F})\,d\Omega = \int_\Gamma \mathbf{F}\cdot s\mathbf{n}\,d\Gamma - \int_\Omega \mathbf{F}\cdot\nabla s\,d\Omega \tag{3.62}$$

and

$$\int_\Omega \mathbf{F}\cdot(\nabla s)\,d\Omega = \int_\Gamma s\mathbf{F}\cdot\mathbf{n}\,d\Gamma - \int_\Omega s\nabla\cdot\mathbf{F}\,d\Omega, \tag{3.63}$$

Before applying the discussed rules for the integration by parts, the term that contains the adjoin quantities $\mathbf{v}$ and q in (3.57) are divided into five separated terms:

(a): $\int_\Omega \mathbf{v}\cdot(\delta\bar{\mathbf{u}}\cdot\nabla)\rho\bar{\mathbf{u}}\,d\Omega$

(b): $\int_\Omega \mathbf{v}\cdot(\rho\bar{\mathbf{u}}\cdot\nabla)\delta\bar{\mathbf{u}}\,d\Omega$

(c): $\int_\Omega q(-\rho\nabla\cdot\delta\bar{\mathbf{u}})\,d\Omega$

(d): $\int_\Omega \mathbf{v}\cdot(\nabla\delta\bar{p})\,d\Omega$

(e): $\int_\Omega \mathbf{v}\cdot(-\nabla\cdot(2\mu D(\delta\bar{\mathbf{u}})))\,d\Omega$

Applying (3.62) to (c) and (3.62) to (d) gives

$$\int_\Omega q(-\rho\nabla\cdot\delta\bar{\mathbf{u}})\, d\Omega = -\int_\Gamma \delta\bar{\mathbf{u}}\cdot\rho q\mathbf{n}\, d\Gamma + \int_\Omega \delta\bar{\mathbf{u}}\cdot\rho\nabla q\, d\Omega \tag{3.64}$$

and

$$\int_\Omega \mathbf{v}\cdot(\nabla\delta\bar{p})\, d\Omega = \int_\Gamma \delta\bar{p}(\mathbf{v}\cdot\mathbf{n})\, d\Gamma - \int_\Omega \delta\bar{p}(\nabla\cdot\mathbf{v})\, d\Omega \tag{3.65}$$

respectively. Using rules from Othmer (2008), the results of integration by parts for (a), (b) and (e) are given by

$$\int_\Omega \mathbf{v}\cdot(\delta\bar{\mathbf{u}}\cdot\nabla)\rho\bar{\mathbf{u}}\, d\Omega = \int_\Gamma \delta\bar{\mathbf{u}}\cdot(\mathbf{n}(\mathbf{v}\cdot\rho\bar{\mathbf{u}}))\, d\Gamma - \int_\Omega \delta\bar{\mathbf{u}}(\nabla\mathbf{v}\cdot\rho\bar{\mathbf{u}})\, d\Omega, \tag{3.66}$$

$$\int_\Omega \mathbf{v}\cdot(\rho\bar{\mathbf{u}}\cdot\nabla)\delta\bar{\mathbf{u}}\, d\Omega = \int_\Gamma \delta\bar{\mathbf{u}}\cdot(\mathbf{v}(\rho\bar{\mathbf{u}}\cdot\mathbf{n}))\, d\Gamma - \int_\Omega \delta\bar{\mathbf{u}}((\rho\bar{\mathbf{u}}\cdot\nabla)\mathbf{v})\, d\Omega, \tag{3.67}$$

$$\begin{aligned}\int_\Omega \mathbf{v}\cdot(-\nabla\cdot(2\mu D(\delta\bar{\mathbf{u}})))\, d\Omega = \int_\Gamma \delta\bar{\mathbf{u}}(2\mu\mathbf{n}\cdot D(\mathbf{v}))\, d\Gamma &- \int_\Gamma (2\mu\mathbf{n}\cdot D(\delta\bar{\mathbf{u}}))\cdot\mathbf{v}\, d\Gamma \\ &- \int_\Omega \delta\bar{\mathbf{u}}(\nabla\cdot 2\mu D(\mathbf{v}))\, d\Omega.\end{aligned} \tag{3.68}$$

Combining the results from (3.66), (3.67), (3.64), (3.65) and (3.68) allows to rewrite (3.57):

$$\begin{aligned}0 = &\int_\Gamma (2\mu\mathbf{n}\cdot D(\delta\bar{\mathbf{u}}))\cdot\mathbf{v}\, d\Gamma \\ &+ \int_\Gamma \begin{pmatrix}\delta\bar{\mathbf{u}}\\ \delta\bar{p}\end{pmatrix}\cdot\begin{pmatrix}\mathbf{n}(\mathbf{v}\cdot\rho\bar{\mathbf{u}}) + \mathbf{v}(\rho\bar{\mathbf{u}}\cdot\mathbf{n}) + 2\mu\mathbf{n}\cdot D(\mathbf{v}) - q\mathbf{n} + \sigma(\bar{\mathbf{u}} - \bar{\mathbf{u}}_{\mathbf{d}})\\ \mathbf{v}\cdot\mathbf{n}\end{pmatrix} d\Gamma \\ &- \int_\Omega \begin{pmatrix}\delta\bar{\mathbf{u}}\\ \delta\bar{p}\end{pmatrix}\cdot\begin{pmatrix}\nabla\mathbf{v}\cdot\rho\bar{\mathbf{u}} + (\rho\bar{\mathbf{u}}\cdot\nabla)\mathbf{v} + \nabla\cdot 2\mu D(\mathbf{v}) - \rho\nabla q + \sigma(\bar{\mathbf{u}} - \bar{\mathbf{u}}_{\mathbf{d}})\\ \nabla\cdot\mathbf{v}\end{pmatrix} d\Omega\end{aligned} \tag{3.69}$$

In order to satisfy the equation (3.69) for any arbitrary variation $(\delta\bar{\mathbf{u}}, \delta\bar{p})^T$, the evaluations of both the volume and surface integrals should be equal to zero. The conditions of which the volume integral becomes zero are

$$\nabla\mathbf{v}\cdot\rho\bar{\mathbf{u}} + (\rho\bar{\mathbf{u}}\cdot\nabla)\mathbf{v} + \nabla\cdot 2\mu D(\mathbf{v}) - \rho\nabla q + \sigma(\bar{\mathbf{u}} - \bar{\mathbf{u}}_{\mathbf{d}}) = 0 \tag{3.70}$$

$$\nabla\cdot\mathbf{v} = 0. \tag{3.71}$$

These conditions are known as the adjoint momentum and continuity equations. The adjoint boundary conditions can be determined by setting the remaining surface integral from (3.69) to be zero such that

$$\int_\Gamma (2\mu\mathbf{n}\cdot D(\delta\bar{\mathbf{u}}))\cdot\mathbf{v} + \delta\bar{\mathbf{u}}\cdot(\mathbf{n}(\mathbf{v}\cdot\rho\bar{\mathbf{u}}) + \mathbf{v}(\rho\bar{\mathbf{u}}\cdot\mathbf{n}) + 2\mu\mathbf{n}\cdot D(\mathbf{v}) - q\mathbf{n} + \sigma(\bar{\mathbf{u}} - \bar{\mathbf{u}}_{\mathbf{d}})) + \delta\bar{p}(\mathbf{v}\cdot\mathbf{n})\, d\Gamma = 0. \tag{3.72}$$

More specific boundary conditions will be discussed when test cases are presented.

Chapter 4

Momentum forcing characterization

Previously in Chapter 3, the full-field inversion technique was discussed to obtain the optimal estimate $\mathbf{f}^*$ for the momentum forcing $\mathbf{f}$. By assuming that the dataset $\mathbf{d}$ describes the high-fidelity behaviour of turbulent flows, $\mathbf{f}^*$ is expected to uniquely represent the divergence of the Reynolds stress tensor:

$$\mathbf{f}^* \approx \nabla \cdot \rho \overline{\mathbf{u}'_\mathbf{d} \mathbf{u}'_\mathbf{d}}. \tag{4.1}$$

However, it is often observed that $\mathbf{f}^*$ unnecessarily includes other influences such as applied momentum sources or pressure gradients, depending on the set-up of flow cases. As a result, the relation (4.1) is not always satisfied by $\mathbf{f}^*$. Dovetta (2014) introduce a method to filter out a momentum source from $\mathbf{f}^*$ and obtain the corrected momentum forcing $\hat{\mathbf{f}}$. Furthermore, they also provide a methodology to extract the shear stress component $\overline{u'v'}$ from the stream-wise momentum forcing $\hat{\mathbf{f}}$. If $\overline{u'v'}$ satisfies the shear stress data of $\mathbf{d}$ such that

$$\overline{u'v'} \approx \overline{u'_\mathbf{d} v'_\mathbf{d}}, \tag{4.2}$$

then the identified $\overline{u'v'}$ become the Reynolds shear stress. This implies that the corrected momentum forcing $\hat{\mathbf{f}}$ can be characterized as the turbulence force. Foures et al. (2014) further develop the technique for the two-dimensional flow problem. Based on their approach, this chapter will describe the process of extracting the shear stress component $\overline{u'v'}$ from the optimal estimate $\mathbf{f}^*$. The description is limited to the wall-bounded flow cases where the flows are driven by a constant momentum source.

4.1 1D flow case

The x-component of the optimal estimate $\mathbf{f}^*$ is decomposed into

$$\mathbf{f}_x^* = \hat{\mathbf{f}}_x + \mathbf{M} \tag{4.3}$$

where $\hat{\mathbf{f}}_x$ is the actual momentum forcing identified and $\mathbf{M}$ is the applied constant momentum source. Using (2.30), $\hat{\mathbf{f}}_x$ can be written as

$$\hat{\mathbf{f}}_x = \rho \frac{\partial(\overline{u'v'})}{\partial y}. \tag{4.4}$$

By referring the methodology of Dovetta (2014), taking the integration of (4.3) over the entire flow domain gives

$$\int_0^\delta \mathbf{f}_x^* \, dy = \int_0^\delta \hat{\mathbf{f}}_x + \mathbf{M} \, dy \qquad\qquad 0 < y < \delta \tag{4.5}$$

where δ indicates the maximum range of the flow domain. Substituting (4.4) into (4.5) leads to

$$\int_0^\delta \mathbf{f}_x^* \, dy = \int_0^\delta \rho \frac{\partial(\overline{u'v'})}{\partial y} + \mathbf{M} \, dy \tag{4.6}$$

$$= \int_0^\delta \rho \frac{\partial(\overline{u'v'})}{\partial y} \, dy + \int_0^\delta \mathbf{M} \, dy \tag{4.7}$$

Due to the transverse shear stress profile along the cross section of the channel, the integral of $\overline{u'v'}$ over the y-axis is zero, which implies

$$\int_0^\delta \rho \frac{\partial(\overline{u'v'})}{\partial y} \, dy = 0. \tag{4.8}$$

Consequently, (4.7) becomes

$$\int_0^\delta \mathbf{f}_x^* \, dy = \int_0^\delta \mathbf{M} \, dy. \tag{4.9}$$

Evaluating the right hand side of (4.9) and rearranging for $\mathbf{M}$ gives

$$\mathbf{M} = \frac{1}{\delta} \int_0^\delta \mathbf{f}_x^* \, dy. \tag{4.10}$$

Substituting (4.10) back into (4.3) gives

$$\hat{\mathbf{f}}_x = \mathbf{f}_x^* - \frac{1}{\delta} \int_0^\delta \mathbf{f}_x^* \, dy. \tag{4.11}$$

Integrating (4.11) with respect to y_i leads to

$$(\overline{u'v'})_i = \frac{1}{\rho}\int_0^{y_i}\left(\mathbf{f}_x^* - \frac{1}{\delta}\int_0^{\delta}\mathbf{f}_x^*\,dy\right)\,dy \tag{4.12}$$

where i indicates the index of each element. Evaluating (4.12) is expected to deliver the Reynolds shear stress for the 1D channel flow case by numerically integrating it with proper boundary conditions.

4.2 2D flow case

In two-dimensional flow case, optimal estimate $\mathbf{f}^*$ can be decomposed into

$$\begin{pmatrix}\mathbf{f}_x^*\\ \mathbf{f}_y^*\end{pmatrix} = \begin{pmatrix}\hat{\mathbf{f}}_x\\ \hat{\mathbf{f}}_y\end{pmatrix} + \begin{pmatrix}\mathbf{M}\\ 0\end{pmatrix} \tag{4.13}$$

where the momentum source $\mathbf{M}$ is applied in stream-wise direction. The actual momentum forcing $\hat{\mathbf{f}}$ for each component can be expressed by

$$\begin{pmatrix}\hat{\mathbf{f}}_x\\ \hat{\mathbf{f}}_y\end{pmatrix} = \nabla\cdot\begin{pmatrix}\rho\overline{u'u'} & \rho\overline{u'v'}\\ \rho\overline{u'v'} & \rho\overline{v'v'}\end{pmatrix}. \tag{4.14}$$

By following the approach of Foures et al. (2014), decomposing the divergence of the Reynolds stress tensor into the divergence of a second-order tensor and the gradient of a scalar function ϕ results in

$$\begin{pmatrix}\hat{\mathbf{f}}_x\\ \hat{\mathbf{f}}_y\end{pmatrix} = -\nabla\cdot\begin{pmatrix}\alpha & \beta\\ \beta & -\alpha\end{pmatrix} - \nabla\phi \tag{4.15}$$

with

$$\alpha = -\frac{\rho}{2}(\overline{u'}^2 - \overline{v'}^2), \qquad \phi = -\frac{\rho}{2}(\overline{u'}^2 + \overline{v'}^2), \qquad \beta = -\rho\overline{u'v'}. \tag{4.16}$$

The pressure gradients are non-zero quantities in the 2D flow problem. Hence, $\nabla\phi$ can be combined with the pressure gradient. This modification results in approximations:

$$\begin{pmatrix}\hat{\mathbf{f}}_x\\ \hat{\mathbf{f}}_y\end{pmatrix} \approx -\nabla\cdot\begin{pmatrix}\alpha & \beta\\ \beta & -\alpha\end{pmatrix} \tag{4.17}$$

and

$$\nabla\bar{p} \approx \nabla\bar{p} - \nabla\phi. \tag{4.18}$$

In order to obtain α and β, Foures et al. (2014) use a minimization problem. First, the residual form of expression from (4.17) can be shown by

$$-\nabla \cdot \begin{pmatrix} \alpha & \beta \\ \beta & -\alpha \end{pmatrix} - \begin{pmatrix} \hat{\mathbf{f}}_x \\ \hat{\mathbf{f}}_y \end{pmatrix} = 0. \tag{4.19}$$

The cost function $\mathcal{G}$ is formulated by

$$\mathcal{G}(\alpha,\beta) = \int_\Omega \left(-\frac{\partial \alpha}{\partial x} - \frac{\partial \beta}{\partial y} - \hat{\mathbf{f}}_x\right)^2 + \left(-\frac{\partial \beta}{\partial x} + \frac{\partial \alpha}{\partial y} - \hat{\mathbf{f}}_y\right)^2 d\Omega. \tag{4.20}$$

As the cost function $\mathcal{G}$ is in a form of the quadratic function, its minimum can be achieved when the gradient is zero. The gradient of the cost function is given by

$$\nabla\mathcal{G}(\alpha,\beta) = \int_\Omega \nabla \left[\left(-\frac{\partial \alpha}{\partial x} - \frac{\partial \beta}{\partial y} - \hat{\mathbf{f}}_x\right)^2\right] + \nabla \left[\left(-\frac{\partial \beta}{\partial x} + \frac{\partial \alpha}{\partial y} - \hat{\mathbf{f}}_y\right)^2\right] d\Omega, \tag{4.21}$$

which becomes zero when satisfying

$$\nabla \left[\left(-\frac{\partial \alpha}{\partial x} - \frac{\partial \beta}{\partial y} - \hat{\mathbf{f}}_x\right)^2\right] = 0, \tag{4.22}$$

$$\nabla \left[\left(-\frac{\partial \beta}{\partial x} + \frac{\partial \alpha}{\partial y} - \hat{\mathbf{f}}_y\right)^2\right] = 0. \tag{4.23}$$

Expanding the left hand sides leads to

$$-\frac{\partial^2 \alpha}{\partial x^2} - \frac{\partial^2 \beta}{\partial x \partial y} - \frac{\partial \hat{\mathbf{f}}_x}{\partial x} = 0, \tag{4.24}$$

$$-\frac{\partial^2 \beta}{\partial x^2} + \frac{\partial^2 \alpha}{\partial x \partial y} - \frac{\partial \hat{\mathbf{f}}_y}{\partial x} = 0, \tag{4.25}$$

$$-\frac{\partial^2 \alpha}{\partial x \partial y} - \frac{\partial^2 \beta}{\partial y^2} - \frac{\partial \hat{\mathbf{f}}_x}{\partial y} = 0, \tag{4.26}$$

$$-\frac{\partial^2 \beta}{\partial x \partial y} + \frac{\partial^2 \alpha}{\partial y^2} - \frac{\partial \hat{\mathbf{f}}_y}{\partial y} = 0. \tag{4.27}$$

Substituting (4.24) and (4.25) into (4.26) and (4.27) respectively results in

$$\nabla^2 \alpha = -\frac{\partial \hat{\mathbf{f}}_x}{\partial x} + \frac{\partial \hat{\mathbf{f}}_y}{\partial y}, \tag{4.28}$$

$$\nabla^2 \beta = -\frac{\partial \hat{\mathbf{f}}_y}{\partial x} - \frac{\partial \hat{\mathbf{f}}_x}{\partial y}. \tag{4.29}$$

Computing the right hand sides of (4.28) and (4.29) allows to solve the Poisson equations for α and β with requiring proper boundary conditions. In (4.16), the Reynolds stress tensor is expressed in terms α and β. However, only β is closely related to the shear stress component $\overline{u'v'}$. Furthermore, an approximation is made by combining $\nabla\phi$ with $\nabla\bar{p}$ during the decomposing process. Therefore, possible errors due to the approximation also can be discussed with the results.

Chapter 5

Implementation

This chapter will discuss the implementation of Chapter 3 and Chapter 4. The quasi-Newton algorithm (L-BFGS-B) from the python optimization library is used for the gradient-base optimization. The flow solvers including the base model, adjoint and Poisson equations are implemented in the OpenFOAM CFD package, a finite-volume code written in C++. The implementation of the flow solvers is based on the modification of the existing OpenFOAM solver **simpleFoam**. In the following sections, the entire workflow of the full-field inversion algorithm is addressed. In addition, the OpenFOAM implementation of the flow solvers is explained with details.

5.1 Optimization workflow

The entire workflow of the gradient-based optimization is described through the flow chart in Figure 5.1. The optimizer takes the cost function J evaluation as an input and determine whether the gradient of J satisfies the convergence criteria (CC). The CC is set up by

$$\frac{J_i - J_{i+1}}{max(|J_i|, |J_{i+1}|, 1)} \leq \text{CC}. \tag{5.1}$$

If the cost function J does not reach the minima, then the optimizer will look for the new search direction and the step length. The search direction is determined based the adjoint sensitivity while line search algorithm continuously estimates the appropriate step length. Subsequently, the design variable $\mathbf{f}$ is iteratively updated by (3.18) until CC is satisfied. When the optimization is converged, the latest update of $\mathbf{f}$ corresponds to the optimal value of $\mathbf{f}$. The top-level optimization algorithm is implemented in a python code as shown in Figure 5.2. The details of the python code can be illustrated through Table 5.1.

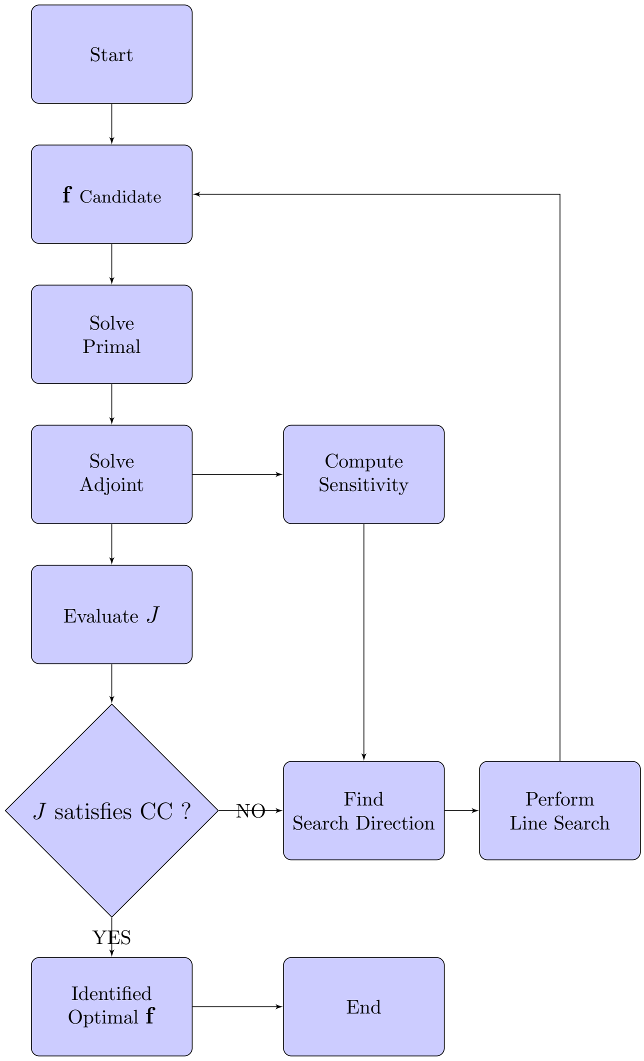

Figure 5.1: Top-Level flow chart for Full-Field Inversion

```
F = F0
opt = {'disp':True, 'factr':10.0}
minimize(costFnc, F, args=(caseDir, 'F', getIndex(), endTime, N),
                              method='L-BFGS-B', jac=gradient, options=opt)
```

Figure 5.2: Top-Level optimization python script

F	momentum forcing **f**
F0	initial guess for **f**
N	grid resolution
disp	set True to print convergence messages
factr	convergence criteria (CC=factr*eps)
eps	machine precision
minimize	scipy.optimize.minimize in python
caseDir	case directory
costFnc	function to compute cost function J
endTime	openFOAM simulation end time
gradient	function to compute adjoint sensitivities

Table 5.1: Illustration of the python code

The second-level implementation computes the adjoint sensitivity and cost function based on the evaluation of primal and adjoint flow quantities. Figure 5.3 shows the implementation of both adjoint sensitivity (3.45) and cost function (3.17). The adjoint sensitivity is implemented in terms of the adjoint velocity of the interior flow domain and the control volume. The implementation is illustrated by in-text comments.

```
while (simple.loop()) // Time loop
{
    Info<< "Time = " << runTime.timeName() << nl << endl;
    {
        // Correcting primal velocity and pressure
            #include "UEqn.H"
            #include "pEqn.H"

        // Correcting for adjoint velocity and pressure
            #include "UaEqn.H"
            #include "paEqn.H"
    }
    // Adjoint sensitivity computation
    // Adjoint velocity Ua and control volume mesh.V
    sens.internalField() = Ua.internalField() * mesh.V();
    runTime.write();
}
// Cost function evaluation via explicit volume integration
// DNS velocity Ud and primal velocity U
costFnc = (fvc::domainIntegrate(0.5*sigma*magSqr(Ud-U))).value();
```

Figure 5.3: Second-level implementation involving sensitivity and cost function computations

5.2 Discretization and implementation of flow solvers

The finite-volume method is one of the most well known discretization techniques in the field of CFD. The idea of the finite-volume method is to locate the quantity of interest at the centre of control volumes and integrate the differential form of governing equations over the each element of control volumes (Moukalled et al., 2015). Integrating the momentum equation (2.31) over the control volume leads to

$$\int_V \rho\nabla\cdot(\bar{\mathbf{u}}\bar{\mathbf{u}}) - \nabla\cdot(2\mu D(\bar{\mathbf{u}})) + \mathbf{f}\,dV = \int_V -\nabla\bar{p}\,dV. \tag{5.2}$$

By using the divergence theorem, (5.2) can be transformed in terms of surface integral

$$\int_S \rho(\bar{\mathbf{u}}\bar{\mathbf{u}})\cdot\mathbf{n} - (2\mu D(\bar{\mathbf{u}}))\cdot\mathbf{n}\,dS + \mathbf{f}V = \int_V -\nabla\bar{p}\,dV, \tag{5.3}$$

which also can be written as semi-discrete form of the momentum equation

$$\sum_j(\rho(\bar{\mathbf{u}}\bar{\mathbf{u}})\cdot\mathbf{n}S)_j - \sum_j((2\mu D(\bar{\mathbf{u}}))\cdot\mathbf{n}S)_j + (\mathbf{f}V)_j = -\left(\int_V \nabla\bar{p}\,dV\right)_j, \tag{5.4}$$

where j indicates the value at any given control volume and surface. First two summation terms can be implicitly solved while the pressure gradient needs to be evaluated explicitly. The OpenFOAM implementation for the primal solver is shown in Figure 5.4. The implementation is illustrated by in-text comments.

```
// Starting primal velocity corrector
// Defining the momentum equation for U
tmp<fvVectorMatrix> UEqn
(
    fvm::div(phi, U)      // Implicit discretization of divergence operator
  - fvm::laplacian(nu, U) // Implicit discretization of laplacian operator
  + F // momentum forcing
  ==
    fvOptions(U) // Applying momentum source using bulk velocity
);

// Under-relax UEqn for U
UEqn().relax();

fvOptions.constrain(UEqn());

// Solving the momentum equation
solve(UEqn() == -fvc::grad(p));

fvOptions.correct(U);
```

Figure 5.4: Primal momentum solver UEqn.H

By following the above discretization steps, integrating the adjoint momentum equation (3.70) over the control volume gives

$$\int_V -\rho\nabla\cdot(\bar{\mathbf{u}}\mathbf{v}) - \rho\nabla\mathbf{v}\cdot\rho\bar{\mathbf{u}} - \nabla\cdot 2\mu D(\mathbf{v}) - \sigma(\bar{\mathbf{u}} - \bar{\mathbf{u}}_{\mathbf{d}})\, dV = -\int_V \rho\nabla q\, dV. \tag{5.5}$$

Applying the divergence theorem leads to

$$\int_S -\rho(\bar{\mathbf{u}}\mathbf{v})\cdot\mathbf{n} - 2\mu D(\mathbf{v})\cdot\mathbf{n}\, dS - \int_V \rho\nabla\mathbf{v}\cdot\rho\bar{\mathbf{u}}\, dV - \sigma(\bar{\mathbf{u}} - \bar{\mathbf{u}}_{\mathbf{d}})V = -\int_V \rho\nabla q\, dV \tag{5.6}$$

and its semi-discrete form becomes

$$\begin{aligned} -\sum_j(\rho(\bar{\mathbf{u}}\mathbf{v})\cdot\mathbf{n}S)_j - \sum_j(2\mu D(\mathbf{v})\cdot\mathbf{n}S)_j \\ -\left(\int_V \rho\nabla\mathbf{v}\cdot\rho\bar{\mathbf{u}}\, dV\right)_j - (\sigma(\bar{\mathbf{u}} - \bar{\mathbf{u}}_{\mathbf{d}})V)_j = -\left(\int_V \rho\nabla q\, dV\right)_j. \end{aligned} \tag{5.7}$$

It is shown that an additional convection term appears in (5.7). Together with the pressure gradient, the adjoint convection term is solved explicitly as shown in Figure 5.5. The implementation is illustrated by in-text comments.

```
// Starting adjoint velocity corrector
// Defining additional convection term
// Using explicit discretization of gradient operator
volVectorField adjointTransposeConvection((fvc::grad(Ua) & U));

// Defining the adjoint momentum equation for Ua
tmp<fvVectorMatrix> UaEqn
(
    fvm::div(-phi, Ua) // Implicit discretization of divergence operator
  - adjointTransposeConvection // additional convection
  - fvm::laplacian(nu, Ua) // Implicit discretization of laplacian operator
  - sigma*(U-Ud) // Result of dJ/dU with sigma=100
  ==
    fvOptions(Ua) // Applying momentum source using bulk velocity
);

// Under - relax UEqn for U
UaEqn().relax();

fvOptions.constrain(UaEqn());

// Solving the momentum equation using explicit discretization of gradient
    operator
solve(UaEqn() == -fvc::grad(pa));

fvOptions.correct(Ua);
```

Figure 5.5: Adjoint momentum solver UaEqn.H

Furthermore, in Chapter 4, the Poisson equations (4.28) and (4.29) are formulated to extract the Reynolds stress tensor components from the optimal estimate $\mathbf{f}^*$. A simple openFOAM implementation of the Poission equations is shown in Figure 5.6. The implementation is illustrated by in-text comments.

```
// Loop correcting non-orthogonality.
while (simple.correctNonOrthogonal())
    {
        // Solving Poisson equations for alpha and beta
        // Using implicit discretization of laplacian operator
        // Dimensioned constant D=1
        solve
        (
            - dFxdx + dFydy - fvm::laplacian(D, alpha)
        );

        solve
        (
            - dFydx - dFxdy - fvm::laplacian(D, beta)
        );
    }
```

Figure 5.6: Poisson solver

Chapter 6

Test cases

The full-field inversion will be tested on two canonical flow cases: the fully developed turbulent flow in a channel and the turbulent flow over periodic hills. The tests are performed based on DNS data for each case. The channel flow data is produced by Lee and Moser (2015) and the flow data over two periodic hills are from Breuer et al. (2009). The momentum forcing $\mathbf{f}$ is inversely estimated by comparing the velocity field produced by the base-model simulation with the DNS data. Therefore, boundary conditions and transport properties for the base-model simulations need to be set up to mimic the DNS set-up. This chapter aims to provide the information of the transport conditions used together with general descriptions of both test cases. At the end of this chapter, the imposed boundary conditions will be discussed.

6.1 1D channel flow

A channel flow is the flow bounded by two parallel walls. When the flow enters the channel with an initial condition, the flow touching the solid surfaces is slowed down due to the molecular viscous influence at the walls. Consequently, the velocity at the main stream increases. The influence of the molecular viscosity initially creates the boundary layers. The thickness of the boundary layers increases with the flow travelling in the x-direction. The illustration of the boundary layer development for the bottom surface is shown in Figure 6.1. As the boundary layers develop, the molecular viscous effect becomes smaller and smaller. When the flow is completely out of controls from the molecular viscous effect, the flow becomes turbulent, which results in the momentum exchange between fast and slow flow regions. The turbulent flow becomes full developed when the velocity statistics due to the momentum exchange no longer vary along the stream-wise direction (Pope, 2000).

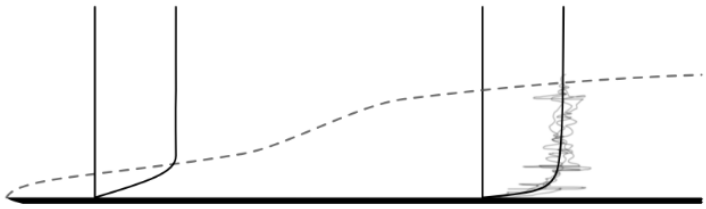

Figure 6.1: Boundary layer development produced by Cleynen (2016)

The 1D fully developed turbulent flow is considered where the flow profiles are no longer influenced by the momentum exchanges. The one-dimensional geometrical set-up is shown in Figure 6.2 where δ is the channel half width. Accordingly, the number of cells is considered only in y-direction. More complex behaviour of the turbulent flow is expected near the walls. Therefore, near-wall grid resolutions need to be achieved to increase the flow convergence. The size of each cell in the y-direction is determined by the simple grading ratio $\mathbf{S}_g$, which represents the ratio of the cell density from the wall to the main stream. Different mesh details and channel geometry information are summarized in Table 6.1.

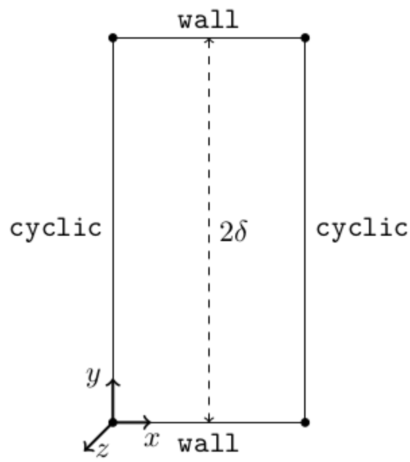

Figure 6.2: OpenFOAM geometrical set-up for 1D channel flow

	fine	medium	coarse	
$\mathbf{N}_y$	320	160	80	
$\mathbf{S}_g$		20 : 1		
δ		1		$[m]$

Table 6.1: Mesh and geometrical details for 1D channel flow

Lee and Moser (2015) provide the details of transport properties they used for their DNS simulations. The Reynolds number $\mathcal{R}e_\tau$ can be defined by

$$\mathcal{R}e_\tau = \frac{u_\tau \delta}{\nu} \tag{6.1}$$

with the kinematic viscosity ν, the channel half width δ and friction velocity u_τ. To mimic the DNS set-up for the given $\mathcal{R}e_\tau$, the bulk velocity $u_\mathbf{b}$ is used together with ν such that

$$\mathcal{R}e_\mathbf{b} = \frac{u_\mathbf{b} \delta}{\nu}. \tag{6.2}$$

Corresponding conditions are summarized in Table 6.2.

$\mathcal{R}e_\tau$	180	550	
u_τ	0.0637309	0.0543496	$[\frac{m}{s}]$
ν	0.00035	0.0001	$[\frac{m^2}{s}]$
$u_\mathbf{b}$	1	1	$[\frac{m}{s}]$

Table 6.2: Transport properties for 1D channel flow

6.2 2D periodic hill flow

The periodic hill flow is also the flow bounded by top and bottom surfaces but the latter surface consists of two hills separated by a certain distance L_x. The main feature of this test case is that the curved geometry of the first hill forces the flow to be separated from the bottom surface. The flow separation is caused by an adverse pressure gradient (Anderson, 2004). To explain the flow separation, let's consider the stream-wise momentum equation within the boundary layer such that

$$\rho \bar{u} \frac{\partial \bar{u}}{\partial x} = -\frac{dp}{dx} + \mu \frac{\partial^2 \bar{u}}{\partial y^2}\bigg|_{y=0}. \tag{6.3}$$

The presence of the adverse pressure gradient ($\frac{dp}{dx} > 0$) causes the stream-wise velocity gradient $\frac{\partial \bar{u}}{\partial x}$ to decrease. When $\frac{\partial \bar{u}}{\partial x}$ eventually becomes zero and change its sign, the flow reversal can be observed. The flow reversal caused by the adverse pressure gradient separates the flow from the bottom surface as illustrated in Figure 6.3. The flow separation additionally creates the recirculation zone in the wake of the flow. The recirculation is closed by the stream line where the flow travels towards a reattachment point. Both the separation and reattachment points can be determined by the locations where

$$\tau_w = \mu \frac{\partial \bar{u}}{\partial y}\bigg|_{y=0} = 0 \tag{6.4}$$

with the wall shear stress τ_w. This will be more extensively discussed when the results of the periodic hill flow is presented.

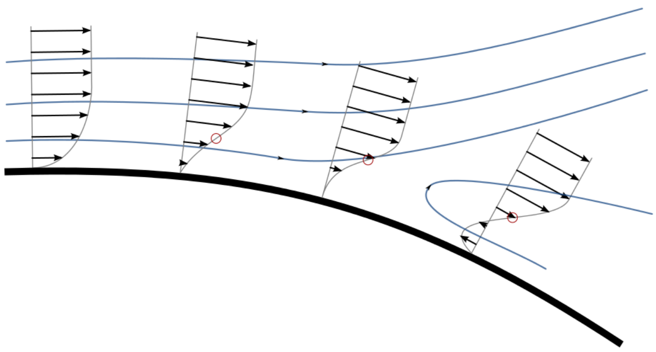

Figure 6.3: Separation of the boundary layer over the curved geometry produced by Cleynen (2016)

The geometrical set-up for the 2D periodic hill flow is shown in Figure 6.4. The constructed mesh details as well as the geometrical information are given in Table 6.3.

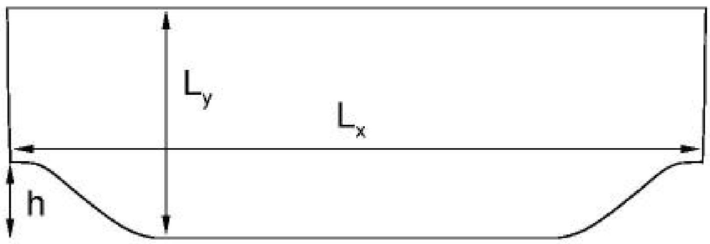

Figure 6.4: Geometrical set-up for 2D periodic hill flow

	fine	medium	coarse	
$\mathbf{N}_x \times \mathbf{N}_y$	200×160	100×80	50×40	
$\mathbf{S}_g$		$20 : 1$		
$\mathrm{L}_x \times \mathrm{L}_y$		9×3.035		$[m^2]$
h		1		$[m]$

Table 6.3: Mesh and geometrical details for 2D periodic hill flow

The DNS flow condition is based on the Reynolds number $\mathcal{R}e$, which is defined by

$$\mathcal{R}e = \frac{u_h \mathrm{L}_y(x=0)}{\nu}, \tag{6.5}$$

which can be related to the bulk velocity Reynolds number $\mathcal{R}e_{\mathbf{b}}$

$$\mathcal{R}e_{\mathbf{b}} = \frac{u_{\mathbf{b}} \mathrm{L}_y(x=0)}{\nu} \tag{6.6}$$

such that

$$\mathcal{R}e_{\mathbf{b}} = \gamma \mathcal{R}e \tag{6.7}$$

where a geometric factor γ is given by

$$\gamma = \frac{\mathrm{L}_y(x=0)}{\frac{1}{\mathrm{L}_x}\int_0^{\mathrm{L}_x} \mathrm{L}_y(x)dx}. \tag{6.8}$$

The transport properties for the periodic hill flow is summarized in Table 6.5. The kinematic viscosity ν is determined based on the given $\mathcal{R}e$.

$\mathcal{R}e$	700	
ν	0.00142857	$[\frac{m^2}{s}]$
u_h	1	$[\frac{m}{s}]$
$u_{\mathbf{b}}$	1	$[\frac{m}{s}]$
γ	0.72	

Table 6.4: Transport properties for 2D periodic hill flow

6.3 Boundary conditions for both cases

Periodic boundary conditions are applied for both test cases introduced in Section 6.1 and Section 6.2. The fully developed velocity profiles at the outlet of the geometries are continuously reimposed at the inlet. The flow bounded by each geometry is no longer driven by the pressure gradient $\nabla \bar{p}$ but by a momentum source $\mathbf{M}$. In OpenFOAM, $\mathbf{M}$ is iteratively corrected during runtime to maintain a certain bulk velocity $u_{\mathbf{b}}$ for both test cases. The imposed $\mathbf{M}$ can be also evaluated through (4.10) using the trapezoidal rule for the numerical integration and will be used to characterize the Reynolds stress tensor components in the result section.

No slip conditions are applied at the walls as Dirichlet boundary conditions. Consequently, there is no momentum at the boundaries, which indicates zero boundary conditions for the momentum forcing $\mathbf{f}$ and the Reynolds stress tensor components. OpenFOAM uses the ρ-normalized boundary conditions for $\mathbf{f}$ and the pressure $\bar{p}$ such that their units follow the normalization:

$$\text{unit of } \rho\text{-normalized } \mathbf{f} \text{ per control volume} = \left[\frac{kg}{m^2 \cdot s^2}\right]\left[\frac{m^3}{kg}\right] = \left[\frac{m}{s^2}\right] \tag{6.9}$$

$$\text{unit of } \rho\text{-normalized } \bar{p} \text{ per control volume} = \left[\frac{kg}{m \cdot s^2}\right]\left[\frac{m^3}{kg}\right] = \left[\frac{m^2}{s^2}\right] \tag{6.10}$$

The unit of the Reynold stress tensor components is the same as the unit of $\bar{p}$. The primal boundary conditions applied for both cases are summarized in table 6.5.

$\bar{\mathbf{u}}$	(0, 0, 0)	$[\frac{m}{s}]$
$\mathbf{f}$	(0, 0, 0)	$[\frac{m}{s^2}]$
$\nabla\bar{p}$	(0, 0, 0)	$[\frac{m}{s^2}]$
$\overline{u'u'}$	0	$[\frac{m^2}{s^2}]$
$\overline{v'v'}$	0	$[\frac{m^2}{s^2}]$
$\overline{u'v'}$	0	$[\frac{m^2}{s^2}]$

Table 6.5: Primal Boundary conditions in OpenFOAM

Additionally, boundary conditions for the adjoint variables $\mathbf{v}$ and q also need to be set. To derive the adjoint boundary conditions, the expression of the surface integral (3.72) is considered. The expression is always satisfied when the inside of the surface integral is zero such that

$$\begin{aligned}&(2\mu\mathbf{n} \cdot D(\delta\bar{\mathbf{u}})) \cdot \mathbf{v} + \delta\bar{p}(\mathbf{v} \cdot \mathbf{n}) + \\ &\quad \delta\bar{\mathbf{u}} \cdot (\mathbf{n}(\mathbf{v} \cdot \rho\bar{\mathbf{u}}) + \mathbf{v}(\rho\bar{\mathbf{u}} \cdot \mathbf{n}) + 2\mu\mathbf{n} \cdot D(\mathbf{v}) - q\mathbf{n} + \sigma(\bar{\mathbf{u}} - \bar{\mathbf{u}}_{\mathbf{d}})) = 0.\end{aligned} \tag{6.11}$$

Let's considered a channel flow simulation where the uniform velocity profile is imposed at the inlet and the velocity gradient is set to be zero at the outlet. Based on the approach of Othmer (2008), no slip condition at the wall and the prescribed velocity profile at the inlet imply no variation of the primal velocity at each boundary such that

$$\delta\bar{\mathbf{u}} = 0. \tag{6.12}$$

This indicates that every terms involved with $\delta\bar{\mathbf{u}}$ will be eliminated from (6.11), thus remaining

$$(2\mu\mathbf{n} \cdot D(\delta\bar{\mathbf{u}})) \cdot \mathbf{v} + \delta\bar{p}(\mathbf{v} \cdot \mathbf{n}) = 0. \tag{6.13}$$

To satisfy (6.13), each term need to be zero independent of any arbitrary variation of the primal flow quantities. For the adiabatic wall, there is no variation of the primal velocity normal to the surface. Therefore, only the tangential component of the primal velocity is remained. Then the remaining conditions are

$$(2\mu\mathbf{n} \cdot D(\delta\bar{\mathbf{u}}_t)) \cdot \mathbf{v}_t = 0 \tag{6.14}$$

and

$$\delta\bar{p}(v_n) = 0 \tag{6.15}$$

with $v_n = \mathbf{v} \cdot \mathbf{n}$. Conditions to satisfy (6.14) and (6.15) for any variation of the primal variables at the inlet and the walls become

$$\mathbf{v}_t = 0, \qquad v_n = 0, \tag{6.16}$$

which are the adjoint velocity boundary conditions. The boundary condition for the adjoint pressure q at the inlet and walls follow the same boundary conditions for the primal pressure $\bar{p}$:

$$\nabla q = 0. \tag{6.17}$$

At the outlet of the channel, imposing the zero primal velocity gradient and zero pressure simplifies (6.11) to

$$\mathbf{n}(\mathbf{v} \cdot \rho\bar{\mathbf{u}}) + \mathbf{v}(\rho\bar{\mathbf{u}} \cdot \mathbf{n}) + 2\mu\mathbf{n} \cdot D(\mathbf{v}) - q\mathbf{n} + \sigma(\bar{\mathbf{u}} - \bar{\mathbf{u}}_{\mathbf{d}}) = 0 \tag{6.18}$$

which can be decomposed into normal and tangential components such that

$$\mathbf{v} \cdot \bar{\mathbf{u}} + v_n\bar{u}_n + \mu(\mathbf{n} \cdot \nabla)v_n - q + \sigma(\bar{\mathbf{u}} - \bar{\mathbf{u}}_{\mathbf{d}}) \cdot \mathbf{n} = 0, \tag{6.19}$$

$$\bar{u}_n\mathbf{v}_t + \mu(\mathbf{n} \cdot \nabla)\mathbf{v}_t + \sigma(\bar{\mathbf{u}} - \bar{\mathbf{u}}_{\mathbf{d}})_t = 0. \tag{6.20}$$

As a consequence, at the outlet, the adjoint pressure condition can be determined by

$$q = \mathbf{v} \cdot \bar{\mathbf{u}} + v_n\bar{u}_n + \mu(\mathbf{n} \cdot \nabla)v_n + \sigma(\bar{\mathbf{u}} - \bar{\mathbf{u}}_{\mathbf{d}}) \cdot \mathbf{n} \tag{6.21}$$

and satisfying (6.20) provides the adjoint velocity boundary conditions. In this thesis, however, the inlet and outlet adjoint boundary conditions are not applicable since periodic boundary conditions are used for both test cases. Applying the periodic boundary conditions allow to avoid the complexity of implementing the adjoint inlet and outelt boundary conditions. Therefore, the adjoint boundary condition is only considered at the wall.

Chapter 7

Results and Analysis

This chapter will present the results of the full-field inversion applied on the turbulent channel flow and the periodic hill flow test cases. First of all, grid convergence studies will be performed to justify the minor influence of the selected grid resolution on simulation results. Subsequently, the results of the base-model simulations with the reduced errors will be illustrated. The characteristics of the identified momentum forcing $\hat{\mathbf{f}}$, which is the corrected form of $\mathbf{f}^*$ from Section 4, will be determined through the DNS data.

7.1 Grid convergence study

In the framework of the full-field inversion, CFD simulations are repeated hundreds or thousands of times. Therefore, the choice of finest grid resolutions may not be the wisest option to avoid the large computational costs. The grid convergence study is a method to investigate the discretization errors of the simulations based on the selected grid resolutions with respect to the finest grids. By following the approach of Roache (1998), the error between the discrete solution and the exact solution is defined as

$$\begin{aligned} E &= g(\Delta y) - g_{exact} \qquad (7.1) \\ &= C_1(\Delta y)^m + C_2(\Delta y)^{m+1} + C_3(\Delta y)^{m+2} + \cdots \qquad (7.2) \end{aligned}$$

where C_i is a constant, Δy is the grid spacing and m is the order of convergence. The contribution of higher order terms is relatively small compared to the term with the order of m. Therefore, all the higher order terms are neglected. Having simplified the error expression, taking the logarithm of both sides of (7.2) leads to

$$\begin{aligned} \log(E) &= \log(C_1(\Delta y)^m) \\ &= \log(C_1) + m\log(\Delta y) \qquad (7.3) \end{aligned}$$

which indicates that the order of convergence can be evaluated by estimating the slope of $\log(E)$ versus $\log(\Delta y)$ plot. Furthermore, the order of convergence can be more directly evaluated by using a constant grid refinement ratio (r) and its expression is given by

$$m = \log\left(\frac{g_3 - g_2}{g_2 - g_1}\right) / \log(r). \tag{7.4}$$

The expression (7.4) is based on three solutions where g_3 corresponds to the solution from the coarsest-grid and g_1 indicates the finest-grid solution. Additionally, a higher-order solution can be further estimated from the obtained lower-order solutions by using Richardson extrapolation. This method allows to acknowledge the discrepancy between the solution at zero grid spacing and the solution at the selected grid. The discrete solution ($g(\Delta y)$) can be expressed by the *Taylor* series expansion

$$g(\Delta y) = g_0 + g'''(\Delta y) + \frac{g'''}{2}(\Delta y)^2 + \frac{g'''}{6}(\Delta y)^3 + \cdots \tag{7.5}$$

where g_0 indicates the solution in the limit of zero grid spacing. Under the assumption that the solution converges with second-order accuracy, the higher-order solution based on the two finest grid solutions can be computed by

$$g_0 \approx g_1 + \frac{g_1 - g_2}{r^m - 1}. \tag{7.6}$$

The grid convergence study starts with determining quantities of interest that are relevant to the test cases introduced. The quantity of interest for the wall bounded cases such as channel flow and periodic hill flow is the wall shear stress τ_w as it continuously varies with grid resolutions. For the one-dimensional channel flow problem, τ_w only exists at the bottom and top walls, and they are also equivalent to each other. On the other hand, the two-dimensional periodic hill case contains a distribution of τ_w in x-direction and geometrical difference between the top and bottom walls. As a consequence, it is most instructive to determine the point location of τ_w for the grid convergence study. τ_w is taken from the bottom wall at the outlet of the flow. The flow simulations for each test case are performed based on the mesh grid given in Table 6.1 and Table 6.3. Since finer grids are constructed near the walls for both cases, Δy is determined by taking the average of entire grid spacings such that

$$\Delta y = \frac{\sum_{i=1}^{\mathbf{N}_y}(y_{c_{i+1}} - y_{c_i})}{\mathbf{N}_y - 1} \tag{7.7}$$

where y_c is the set of centre coordinates of grid cells in y-direction. Normalizing Δy by the smallest average-grid spacing gives

$$(\Delta y)^+ = \frac{\Delta y}{\Delta y_{\text{smallest}}} \tag{7.8}$$

The evaluations of τ_w together with $(\Delta y)^+$ for each test case are given in Table 7.1 and 7.2.

Table 7.1: Evaluation of τ_w for one-dimensional channel flow

$\mathbf{N}_y$	Δy	$(\Delta y)^+$	τ_w
320	0.006267	1.00	-0.00104993
160	0.012566	2.01	-0.00104971
80	0.025267	4.03	-0.00104881

Table 7.2: Evaluation of τ_w for two-dimensional periodic hill flow

$\mathbf{N}_y$	Δy	$(\Delta y)^+$	τ_w
200	0.012786	1.00	-0.01212630
100	0.025709	2.01	-0.01283799
50	0.052042	4.07	-0.027923

The order of convergence m for τ_w is evaluated using (7.4) and the Richardson extrapolation estimate g_0 is determined by (7.6). The results of the grid convergence study are given in Table 7.3 and the study is visualized through Figure 7.1 and Figure 7.2. Strong convergences for both cases are illustrated by the order of convergence equal or above 2 for τ_w. From the grid convergence studies, it can be seen that the influence of the selected grid resolutions, which correspond to $(\Delta y)^+ = 2$, on the evaluation of τ_w is rather minor. Thus the choice of the grid resolutions can be justified for the use in the flow simulations.

Table 7.3: Results of grid convergence study for both cases

	channel flow	periodic hill flow
m	2	4
g_0	-0.00105	-0.012091

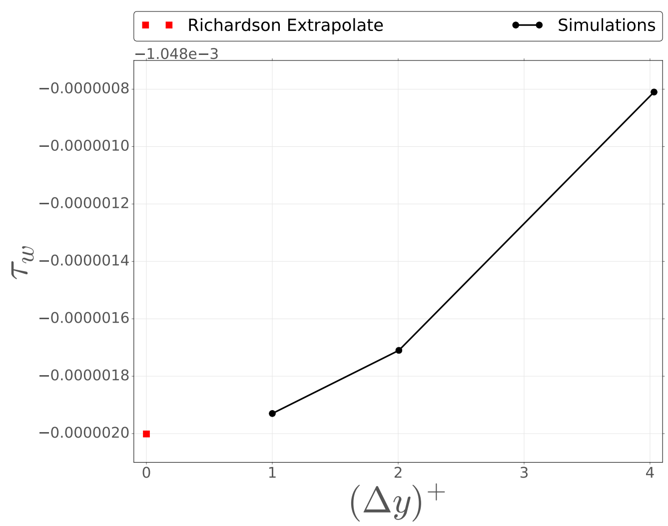

Figure 7.1: Wall shear stress τ_w for the 1D channel flow case with different grid resolutions

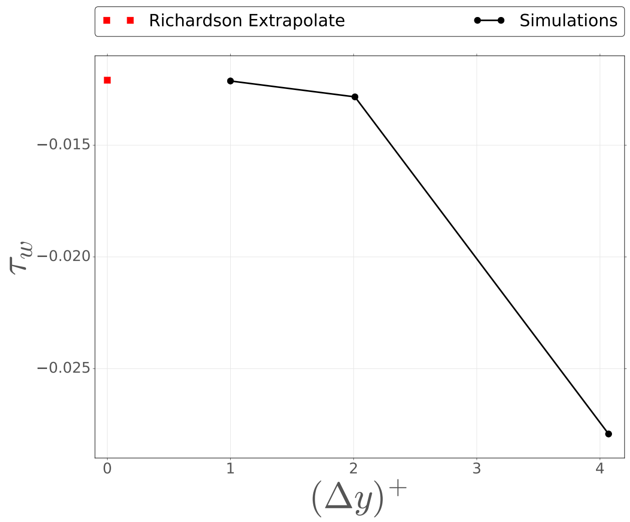

Figure 7.2: Wall shear stress τ_w for 2D periodic hill flow case with different grid resolutions

7.2 1D channel flow results

The results of the full-field inversion applied on the channel flow case will be illustrated in this section. Some of the results are presented in non-dimensional forms. The dimensionless quantities used in this section are given by

$$y^+ = \frac{yu_\tau}{\nu}, \qquad \bar{u}^+ = \frac{\bar{u}}{u_\tau}, \qquad \overline{u'v'}^+ = \frac{\overline{u'v'}}{u_\tau^2} \tag{7.9}$$

Where the friction velocity u_τ can be evaluated based on the wall shear stress τ_w by

$$u_\tau = \sqrt{\frac{\tau_w}{\rho}} \tag{7.10}$$

To begin with, the result of the optimization for different $\mathcal{R}e_\tau$ is shown in Figure 7.3. The cost function J for both $\mathcal{R}e_\tau$ is successfully minimized based on the adjoint sensitivities. The significant difference is observed in terms of the number of the cost function evaluations between the two cases. The increase of the Reynolds number generally requires longer simulation time. It can be seen that this also complicates the optimization process. The scalar representation σ of the diagonal inverse of the covariance matrix plays a role of the relaxation constant within the cost function J as given in (3.16). The choice of σ is 100, which is determined based on trials and errors to extend the number of optimization runs.

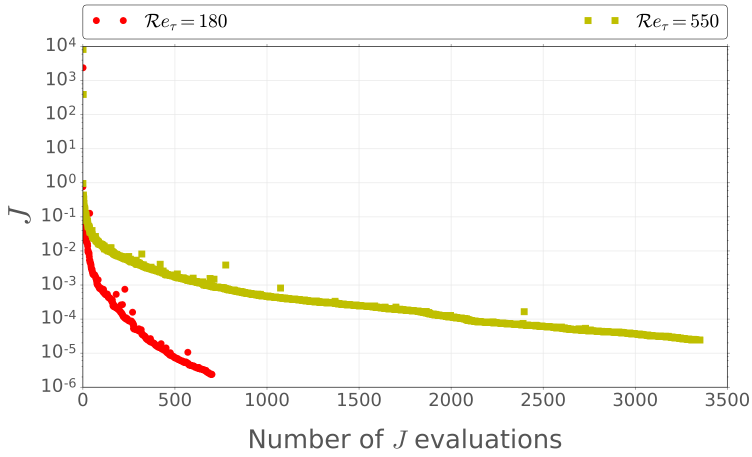

Figure 7.3: Cost function J histories for the 1D channel flow case with different $\mathcal{R}e_\tau$

The reduction in the cost function J is reflected in the result of velocity profiles in Figure 7.4 and 7.5. The base-model with $\mathbf{f}_x = 0$ generates the laminar flow velocity profile. The momentum forcing $\mathbf{f}_x$ is iteratively updated through the full-field inversion. When $\mathbf{f}_x$ reaches to its optimal $\hat{\mathbf{f}}_x$, the velocity difference between the base-model and the mean DNS velocity data is significantly reduced. The near-wall velocity profile for $\mathcal{R}e_\tau = 180$ is more accurately achieved compared to $\mathcal{R}e_\tau = 550$. This is because the lower optimization convergence is resulted with the higher $\mathcal{R}e_\tau$. Improving the optimization convergence still remains as challenge, hence requiring further studies.

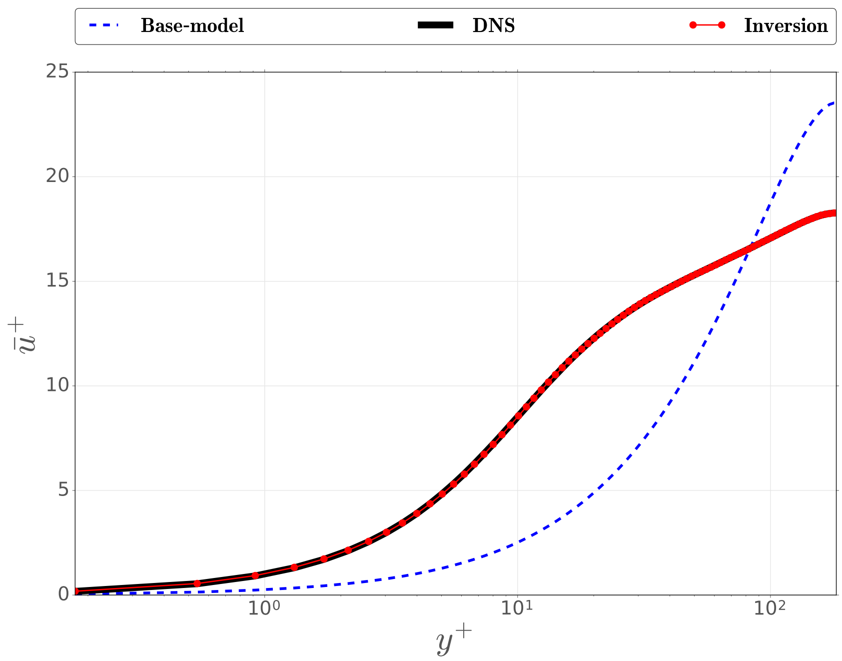

Figure 7.4: Velocity profiles for the 1D channel flow case with $\mathcal{R}e_\tau = 180$

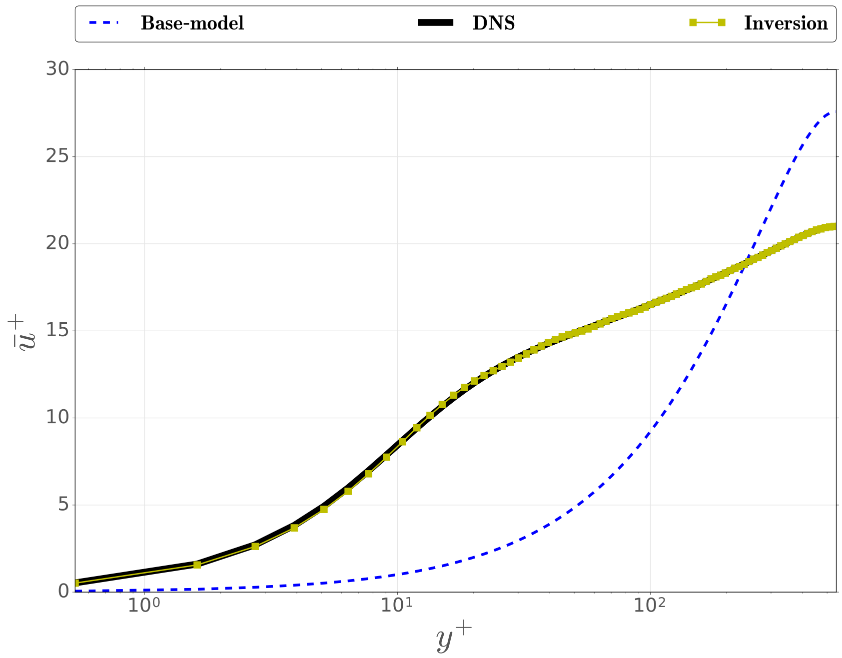

Figure 7.5: Velocity profiles for the 1D channel flow case with $\mathcal{R}e_\tau = 550$

The difference in the y^+ range is observed from the results. The increase in $\mathcal{R}e_\tau$ indicates that the inertial force becomes more dominating the viscous force. The increase of the inertial force results in the steeper velocity gradient at the wall, thus increasing the wall shear stress τ_w. Since y^+ relies on τ_w, higher $\mathcal{R}e_\tau$ leads to the increase of y^+.

The force profiles are compared in Figure 7.6 and Figure 7.7. Although the identified momentum forcing profile $\hat{\mathbf{f}}_x$ have shown a descent agreement with the DNS turbulence force profile at $y^+ \geq 10$, some deviations are also observed near the wall. It is interesting to see that the velocity field produced by the full-field inversion is still strongly converged to the mean DNS velocity data despite the force profile deviations.

To investigate further on the characteristics of the identified momentum forcing profile $\hat{\mathbf{f}}_x$, the shear stress component $\overline{u'v'}$ is extracted from $\hat{\mathbf{f}}_x$ using the expression (4.12). Initially the divergence of the Reynolds stress tensor was replaced by the momentum forcing $\mathbf{f}$ in Section 2.3. If the extracted $\overline{u'v'}$ agrees with the DNS Reynolds shear stress profiles, then the identified $\hat{\mathbf{f}}_x$ represents the DNS turbulence force. Using the boundary conditions given in Table 6.5, the shear stress profiles are compared in Figure 7.8 and 7.9. It can be seen that the deviations observed in the force profiles are significantly reduced in the shear stress profiles for both $\mathcal{R}e_\tau$ cases through the characterization process (4.12). As a result, the extracted shear stress $\overline{u'v'}$ strongly agrees with the DNS Reynolds shear stress. This means that the identified momentum forcing $\hat{\mathbf{f}}_x$ contains the turbulence characteristics.

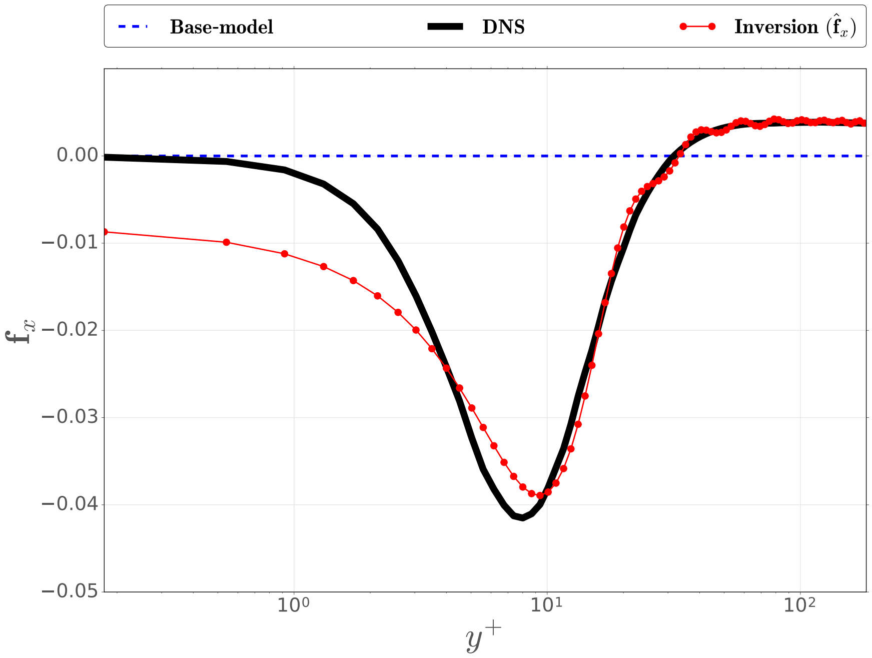

Figure 7.6: Force profiles for the 1D channel flow case with $\mathcal{R}e_\tau = 180$

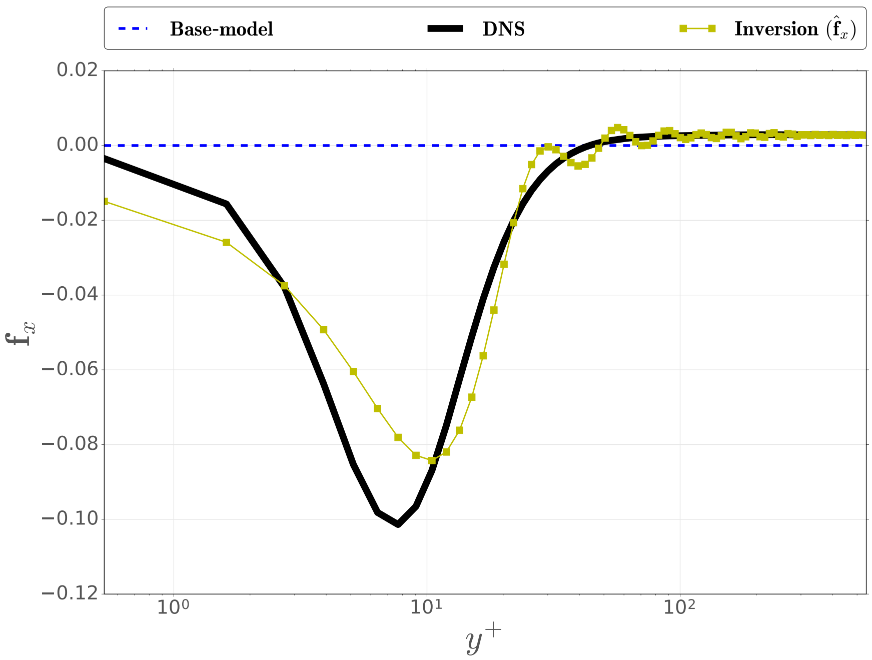

Figure 7.7: Force profiles for the 1D channel flow case with $\mathcal{R}e_\tau = 550$

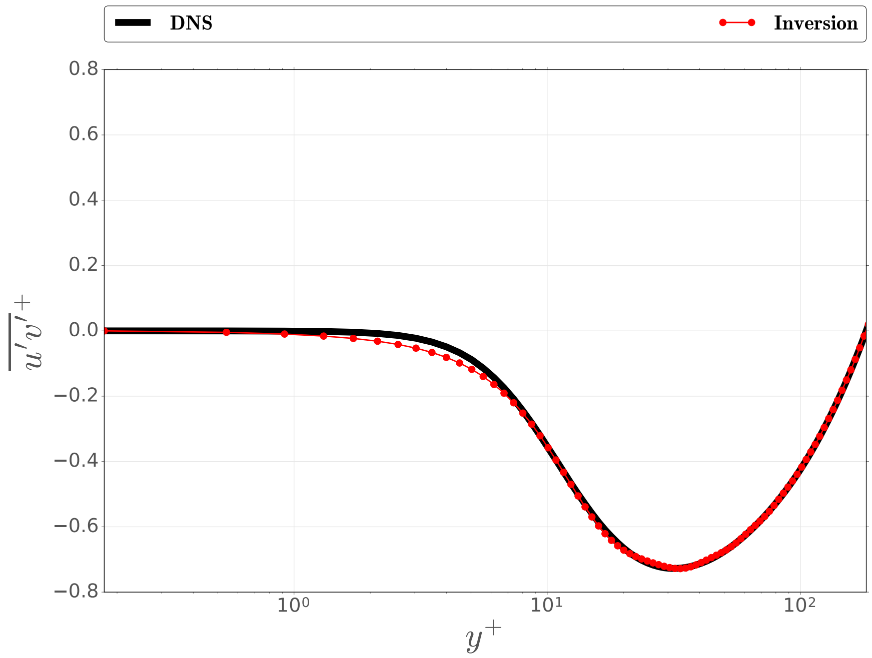

Figure 7.8: Shear stress profiles for the 1D channel flow case with $\mathcal{R}e_\tau = 180$

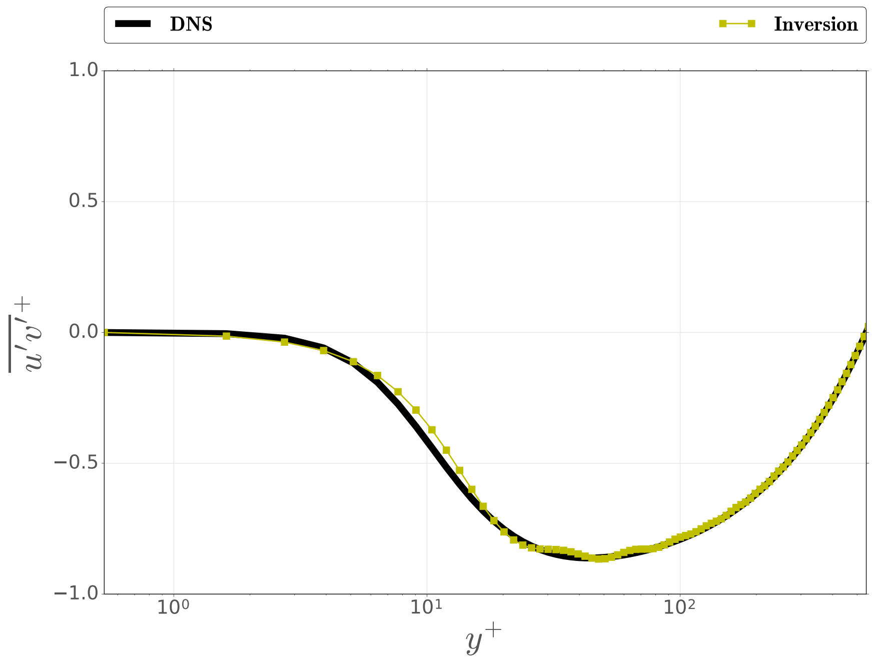

Figure 7.9: Shear stress profiles for the 1D channel flow case with $\mathcal{R}e_\tau = 550$

Another interesting feature of the identified profile $\hat{\mathbf{f}}_x$ is the low-frequency oscillations at $y^+ \geq 30$. The oscillation seems to be magnified with the $\mathcal{R}e_\tau$ case. This feature is suspected as a result of either numerical errors or physical observations. One of the possible causes for the numerical errors is the discontinuity due to the interpolation. If the DNS data is interpolated on the finer grid than its own, then the interpolation will create additional data points that are not necessarily on the trend line of the DNS data. This eventually causes the discontinuity. Fortunately, this is not the case since the DNS data is on much finer grid than the base-model simulation. Another cause of the numerical errors is the choice of the grid resolution. The influence of the grid resolution on the flow simulations was previously discussed in Section 7.1. To investigate whether the grid resolution influences on the results of the optimization, the full-field inversion is further performed with lower and higher grid configurations. The results for the different grid resolutions are summarized through Figure 7.10 and Figure 7.11. No significant difference among different grid configurations is found in regards to the cost function histories and the optimal momentum forcing $\hat{\mathbf{f}}_x$. The low-frequency oscillations also remain the same for the different grid configurations. Therefore, it can be analysed that the oscillating behaviour of $\hat{\mathbf{f}}_x$ is not caused by the numerical errors but possibly interpreted as physical observations, which need to be further investigated in future work.

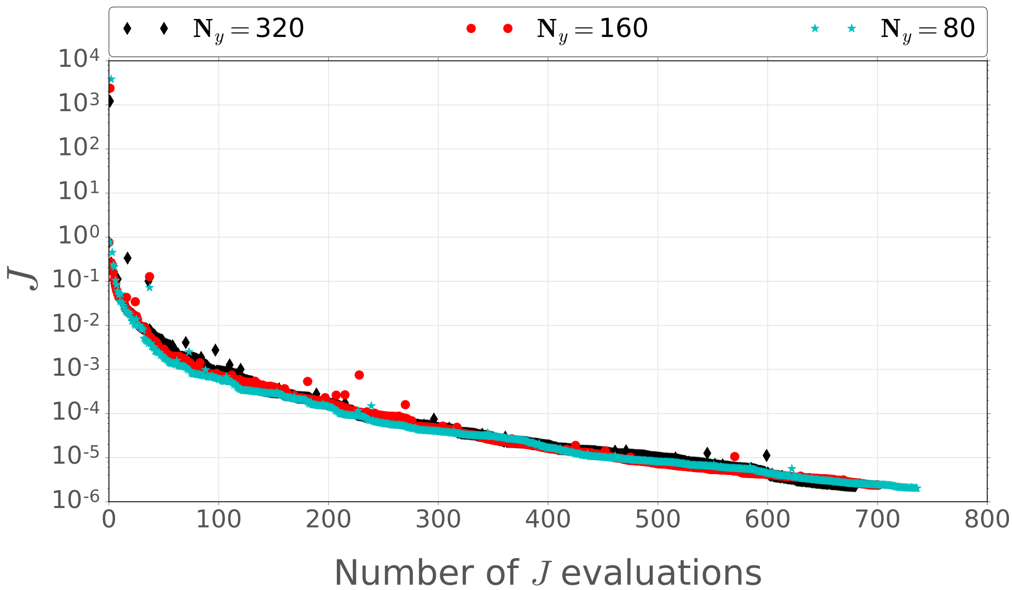

Figure 7.10: Cost function J for the 1D channel flow case with different grid resolutions

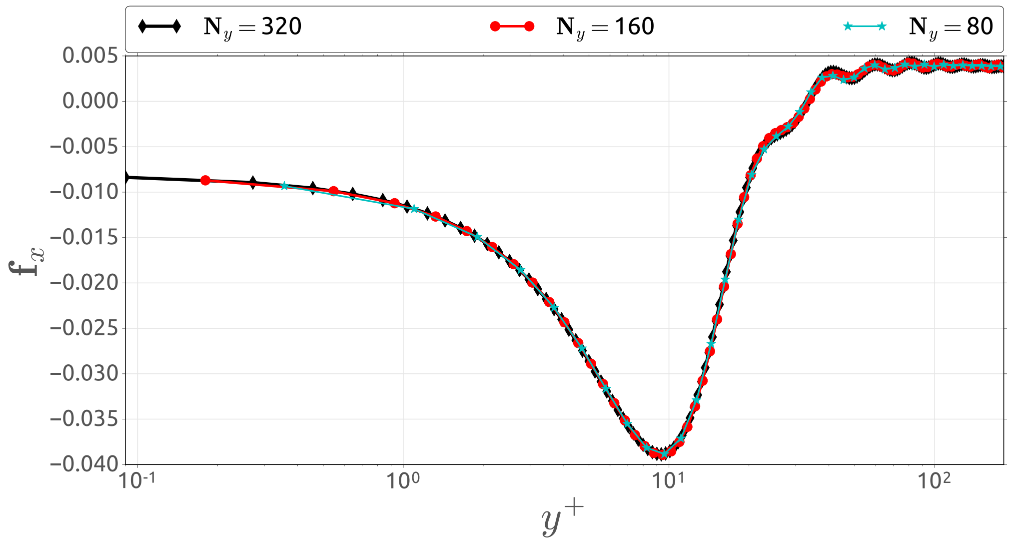

Figure 7.11: Influence of grid resolutions on force profiles for the 1D channel flow case

7.3 2D periodic hill flow results

The full-field inversion is also applied to reduce the base-model simulation errors for the flow over the periodic hills. The choice of initial $\mathbf{f}$ is made by

$$\mathbf{f} = -\mu_t D(\bar{\mathbf{u}})\Big|_{k-\epsilon} \tag{7.11}$$

where the eddy viscosity μ_t and the strain-rate tensor field $D(\bar{\mathbf{u}})$ are computed based on the Launder-Sharma $k-\epsilon$ model. By correcting $\mathbf{f}$ through the full-field inversion, the mean DNS velocity profile is aimed to be achieved. The low Reynolds number $\mathcal{R}e = 700$ is considered. The case of the periodic hill flow requires sufficient grid resolutions to observe the flow separation and recirculation. Therefore, the flow simulation time is expected to take longer compared to the 1D channel flow. The choice of the low $\mathcal{R}e$ is to perform the fundamental studies on how the flow separation influences the result of this framework with the reduced computational burden.

The evaluation history of the cost function J is shown in Figure 7.12. Compared to the 1D channel flow case, the lower rate of the optimization convergence is achieved. The cost function J is reduced based on the adjoint sensitivities and the quasi-Newton optimization algorithm. Since they are complicatedly involved in the gradient-based optimization, it is difficult to determine the exact cause of limiting the J convergence.

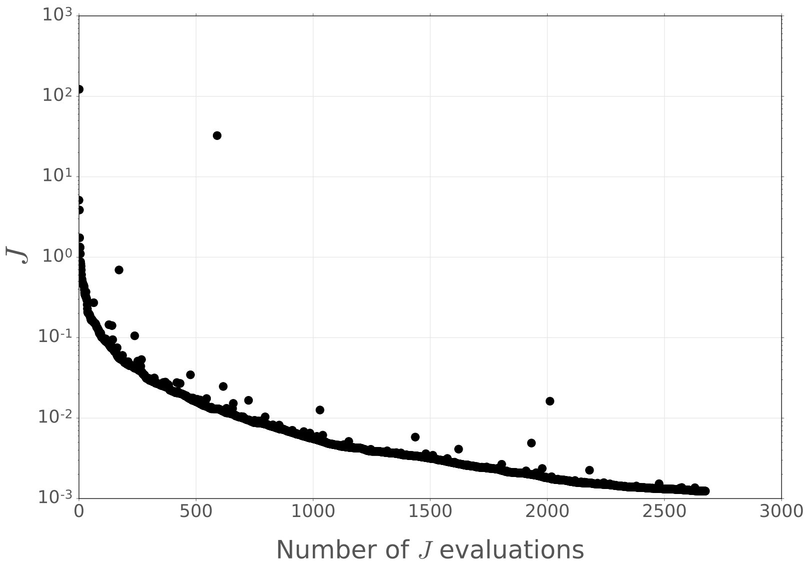

Figure 7.12: Cost function J for the 2D periodic hill flow case

The results of velocity fields are normalized by the bulk velocity $u_{\mathbf{b}}$, scaled by 2 and presented in Figure 7.13 and Figure 7.14. Despite the reduced rate of the J convergence, the result shows that difference between the Launder-Sharma $k-\epsilon$ base-model solution and the mean DNS velocity data is remarkably reduced by applying the full-field inversion. Moreover, the feature of the flow reversal within the recirculation zone is also accurately achieved with respect to the mean DNS velocity data.

Another interesting quantity of interest in the periodic hill flow case is the wall shear stress τ_w. When the flow is separated from the bottom surface, the velocity gradient becomes zero at the wall. Since τ_w is defined by

$$\tau_w = \left.\frac{\partial \bar{u}}{\partial y}\right|_{wall} \tag{7.12}$$

the location of the flow separation can be determined when $\tau_w = 0$. The region where the flow is reattached to the bottom surface can be also determined by the same analogy. Figure 7.15 shows the τ_w profiles along the bottom surface in the stream-wise direction. One of the downside of the Launder-Sharma $k-\epsilon$ model is shown to be the limited capability of predicting the flow separation and reattachment points. Although the correction of the inlet and outlet τ_w profiles is not accurately made, the locations of the flow separation and reattachment are more precisely evaluated through the full-field inversion. It is remarkable to see that the flow separation and reattachment features are correctly captured by reducing the errors in the velocity fields. However, improving the τ_w estimation at the inlet and the outlet of the flow domain still remains as challenge.

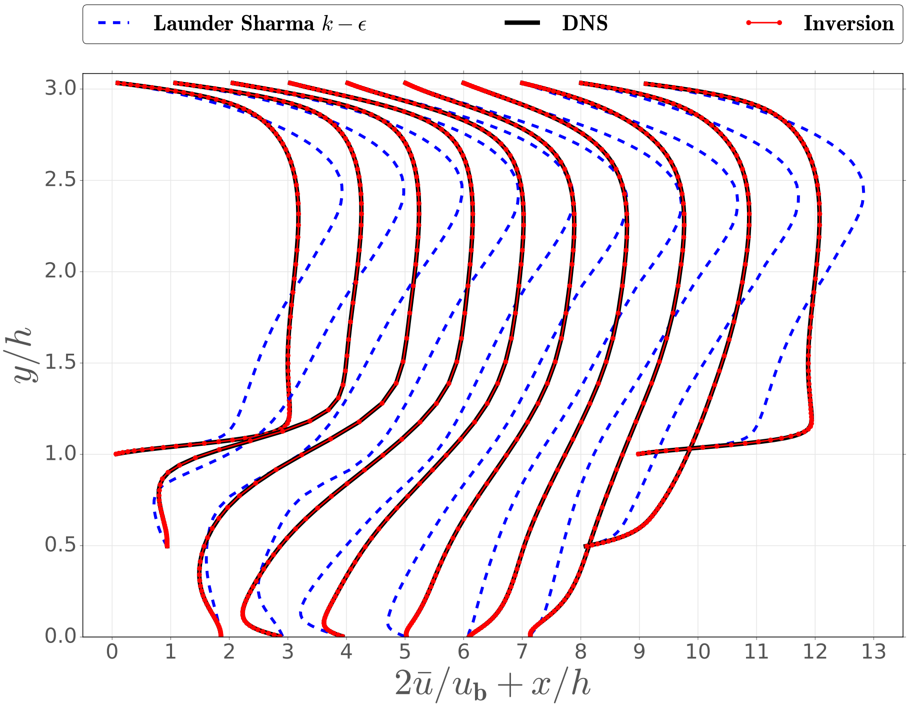

Figure 7.13: Velocity profiles in x-direction for the 2D periodic hill flow case

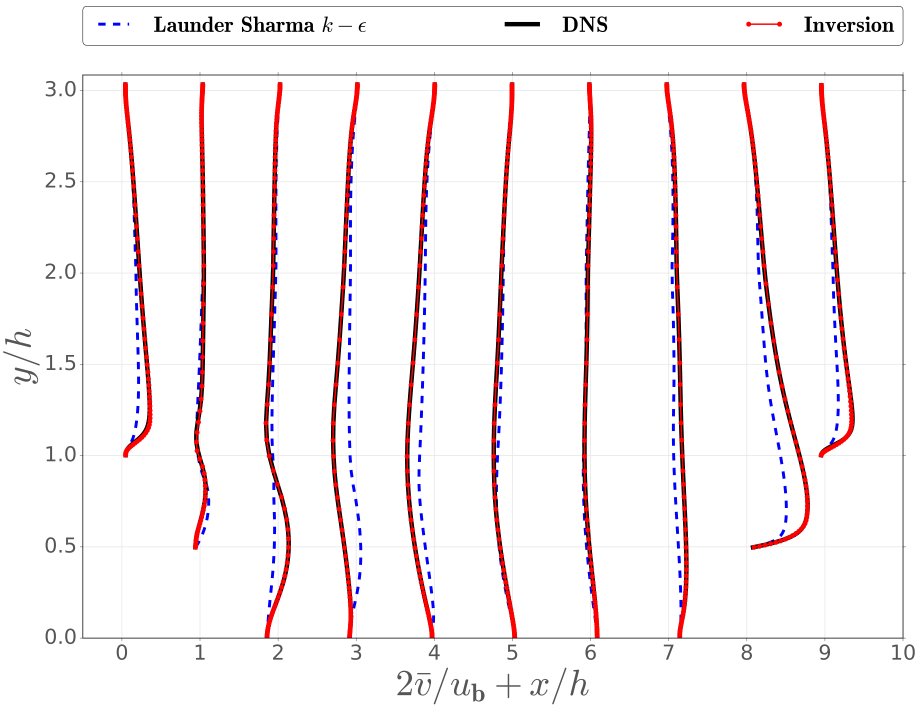

Figure 7.14: Velocity profiles in y-direction for the 2D periodic hill flow case

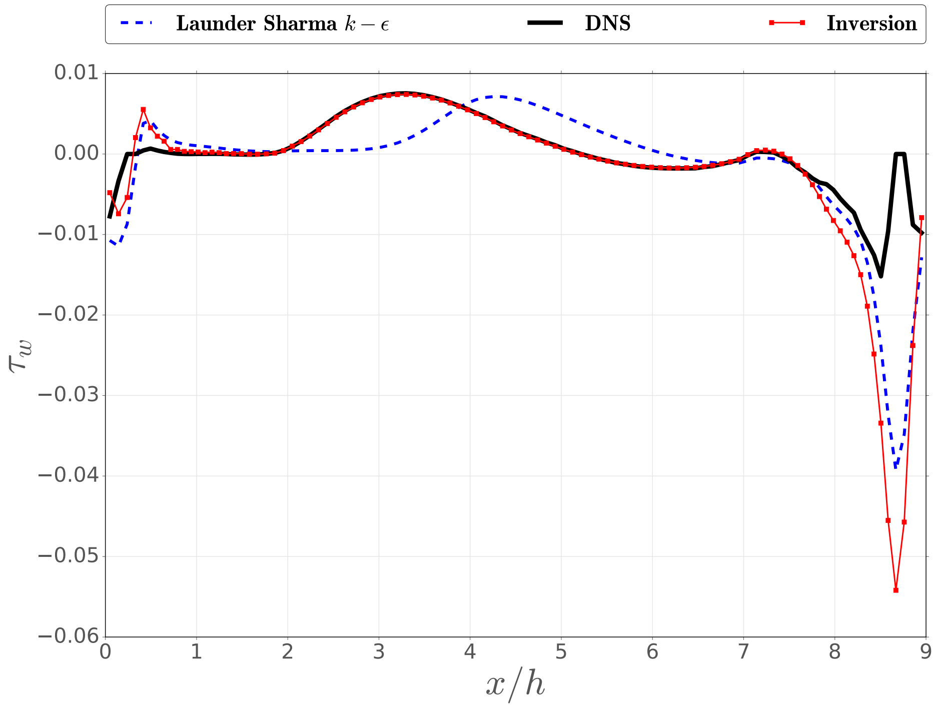

Figure 7.15: Wall shear stress τ_w profiles along the bottom surface

The optimal momentum forcing $\hat{\mathbf{f}}$ is the result of iteratively correcting $\mathbf{f}$ by demanding the error reductions in the velocity field of the Launder-Sharma $k-\epsilon$ base-model. Different force profiles are compared through Figure 7.16 and Figure 7.17. The force profiles both in x- and y-direction are scaled by 5. Unlikely to the velocity profiles from Figure 7.13 and Figure 7.14, substantial differences are still observed between the identified $\hat{\mathbf{f}}$ and the DNS turbulence force.

The deviations from the DNS turbulence force can be analysed through the wall shear stress τ_w given in Figure 7.15. The flow separation near the first curvature has the negative influence on $\hat{\mathbf{f}}$. As the flow travels over the recirculation zone, the deviations in the force profiles become diminished. The minimal deviations are observed when the flow is reattached to the bottom surface. The reattachment point also can be considered as the region where the the influence of the flow separation is minimum. Consequently, it can be seen that the predominant cause of the deviations in the force profiles is the flow separation.

More substantial deviations are observed in the y component of the force profiles compared to their x component. Figure 7.14 shows that almost no improvement is made by the full-field inversion. This indicates that the x component of the optimal momentum forcing $\hat{\mathbf{f}}$ has more dominant influences on the velocity field. Similar to the 1D channel flow case, the behaviour of $\hat{\mathbf{f}}$ is still capable of reproducing the mean DNS velocity field in spite of the observed deviations in the force profiles.

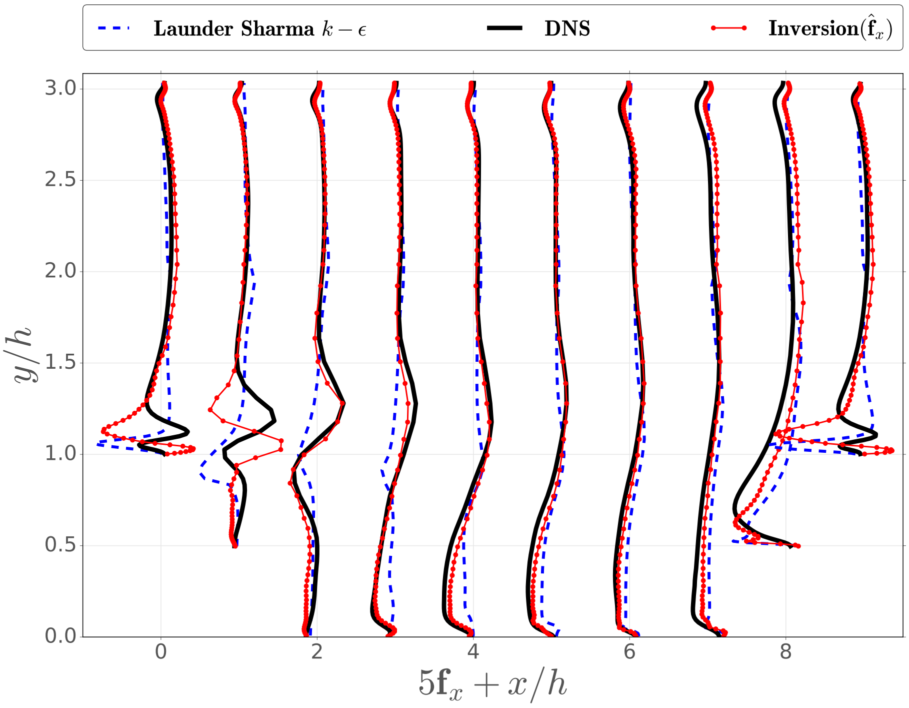

Figure 7.16: Force profiles in x-direction for the 2D periodic hill flow case

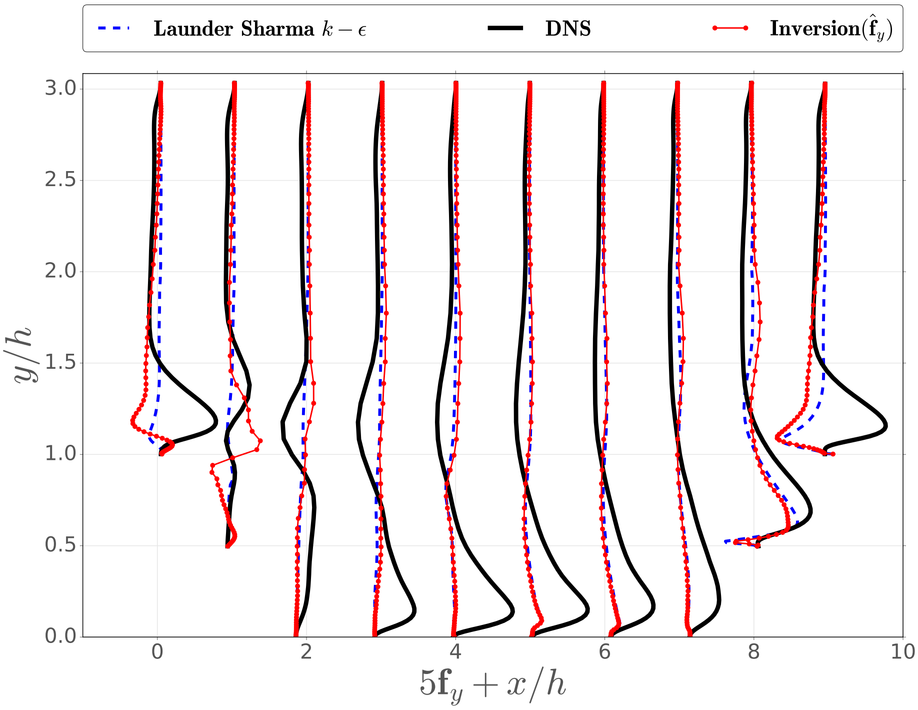

Figure 7.17: Force profiles in y-direction for the 2D periodic hill flow case

The characteristics of the identified momentum forcing $\hat{\mathbf{f}}_x$ is further investigated by making the comparison in shear stress profiles. By following the approach discussed in Section 4.2, the Poisson equation (4.29) with the boundary conditions from Table 6.5 is solved to extract the shear stress representation β from $\hat{\mathbf{f}}_x$. If the extracted β profiles agrees with the DNS Reynolds shear stress, then the identified momentum forcing $\hat{\mathbf{f}}_x$ represents the stream-wise DNS turbulence force.

The extracted shear stress β is compared with the Launder-Sharma $k-\epsilon$ and the DNS Reynolds shear stress profiles in Figure 7.18. The shear stress profiles are normalized by a square of the bulk velocity $u_\mathbf{b}$ and scaled by 7. The shear stress profile of the Launder-Sharma $k-\epsilon$ is slight improved towards the DNS shear stress profile through the full-field inversion. The deviations observed in the force profiles from Figure 7.16 are also dwindled. However, the characterization process does not significantly reduce the deviations, thus remaining the interrupted β profiles due to the flow separation.

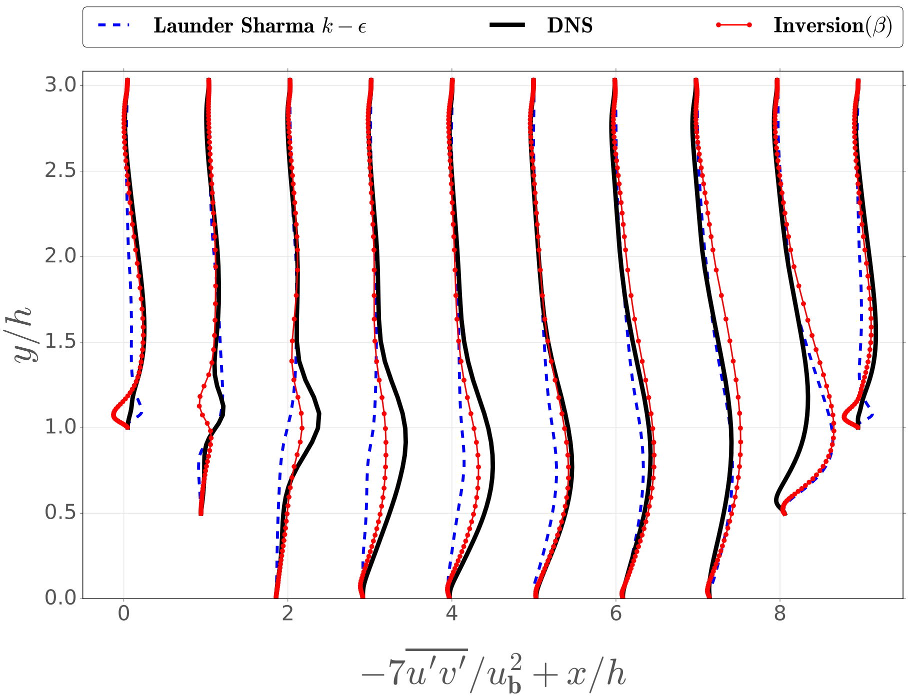

Figure 7.18: Shear stress profiles for the 2D periodic hill flow case

The flow separation has been discussed as the main cause of the deviations in the shear stress profiles as well as in the force profiles. Additional potential cause can arise from the approximation made during the characterization process. From (4.15), the optimal momentum forcing $\hat{\mathbf{f}}$ is decomposed into the divergence of the modified Reynolds stress tensor and the gradient of the scalar function ϕ. The approximation is made by eliminating $\nabla\phi$ from $\hat{\mathbf{f}}$ such that

$$
\begin{pmatrix} \hat{\mathbf{f}}_x \\ \hat{\mathbf{f}}_y \end{pmatrix} = -\nabla \cdot \begin{pmatrix} \alpha & \beta \\ \beta & -\alpha \end{pmatrix} - \nabla \phi \tag{7.13}
$$

$$
\approx -\nabla \cdot \begin{pmatrix} \alpha & \beta \\ \beta & -\alpha \end{pmatrix}. \tag{7.14}
$$

The eliminated $\nabla\phi$ is combined with the $\nabla\bar{p}$ in the base-model momentum equation, thus forming the modified pressure gradient (4.18). This thesis has not investigated how the modification made with $\nabla\phi$ influences on β. Characterizing $\nabla\phi$ remains as future studies which could increase the capability of the characterization technique proposed by Foures et al. (2014).

Chapter 8

Adjoint sensitivity validation

The momentum forcing $\mathbf{f}$ is a force field that needs to be evaluated at every control volume. Therefore, when $\mathbf{f}$ is considered as a design variable, solving the optimization problem encounters the high-dimensional problem. As a solution to the high-dimensional optimization problem, the continuous adjoint method is considered. The results presented in Chapter 7 are achieved based on the adjoint-based optimization. In the adjoint-based optimization, the cost function J is minimized based on the adjoint sensitivities. While other gradient computation methods such as the finite-different approximation demand one flow field calculation to evaluate the gradient of the cost function J at a particular point location, the entire sensitivity field can be computed by the adjoint method.

The continuous adjoint method is used to solve the optimization problem in this thesis. The method, however, involves complex derivations and has not been tested in various cases. Therefore, it is difficult to determine the validity of the adjoint sensitivities. One way to validate the adjoint sensitivities is the validation through the finite-different gradients. In this chapter, the adjoint sensitivities will be compared with the finite-difference gradients for both test cases. Moreover, the validation process will be additional performed on the different adjoint framework where the *frozen turbulence* assumption is involved.

8.1 Finite-Difference gradient

Based on the procedure discussed in Subsection 3.4.1, the finite-difference gradients for the 1D channel flow problem are determined through Figure 8.1. The gradients are evaluated at seven different y locations. The results show that the truncation errors are added to the gradients when the step size $\Delta\mathbf{f}$ is chosen to be too large while the rounding errors are caused by small $\Delta\mathbf{f}$. This means that minimum errors occur at the region where the variation of the gradients with respect to $\Delta\mathbf{f}$ is minimum. The choice of the finite-difference gradient is made within the minimum error region.

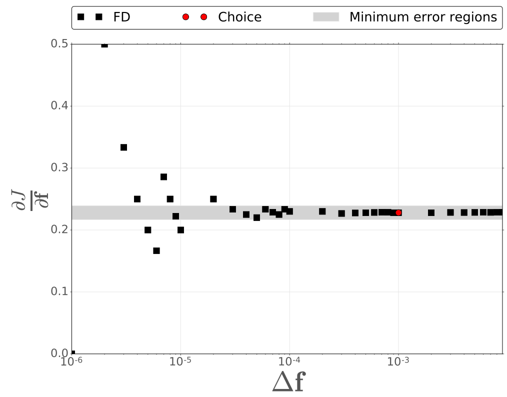

(a) at $\frac{y}{\delta} = 0.025$

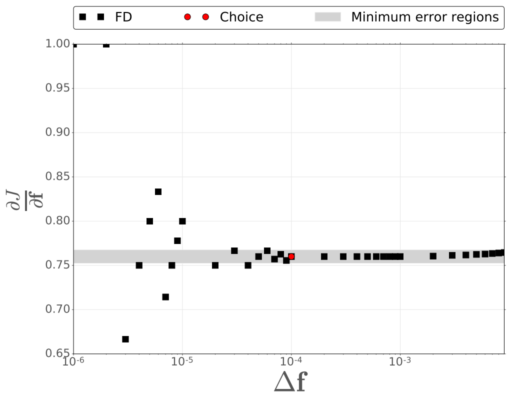

(b) at $\frac{y}{\delta} = 0.059$

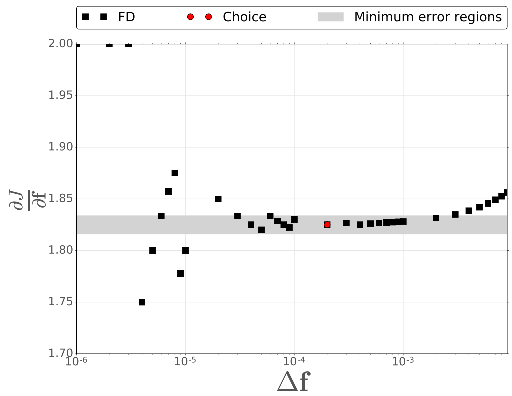

(c) at $\frac{y}{\delta} = 0.110$

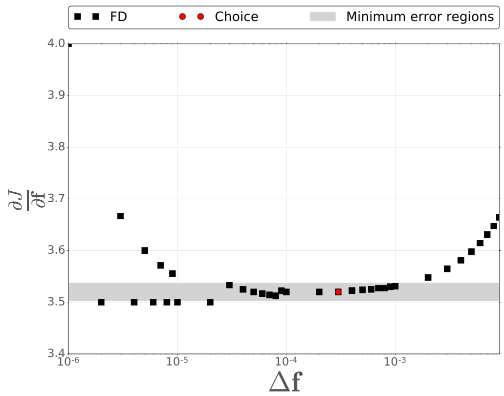

(d) at $\frac{y}{\delta} = 0.184$

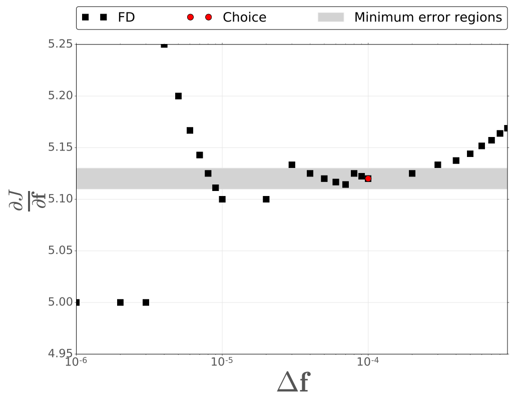

(e) at $\frac{y}{\delta} = 0.293$

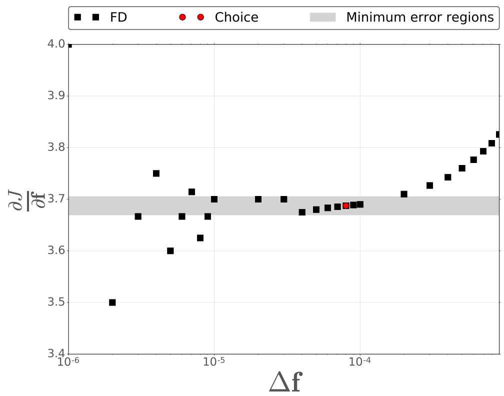

(f) at $\frac{y}{\delta} = 0.451$

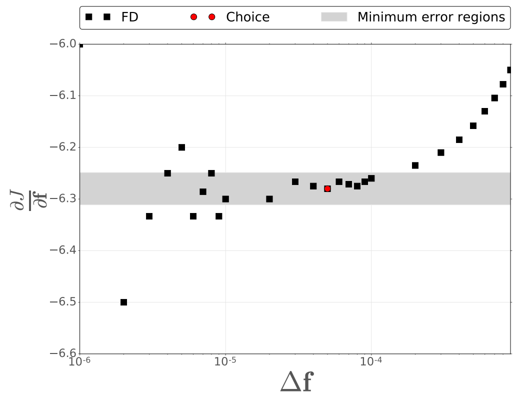

(g) at $\frac{y}{\delta} = 0.682$

Figure 8.1: Determination of finite-difference gradients for the 1D channel flow case

It is shown that the finite-difference approach requires multiple flow calculations only to determine the proper step size $\mathbf{\Delta f}$ for the gradient of the cost function J at a particular point location. Through the entire process illustrated in Figure 8.1, the gradients are determined only for the seven locations. The same procedures are applied to compute the finite-difference gradients for the 2D periodic hill flow case.

8.2 Adjoint vs Finite-Difference

The computation of the adjoint sensitivities is performed using (3.45) and the finite-difference gradients at point locations are determined in Section 8.1. The adjoint sensitivities are compared with the finite-difference gradients for the 1D channel flow in Figure 8.2. The result shows that the adjoint sensitivities strongly agree with the finite-difference gradients. This implies the promising credibility of this adjoint framework for the 1D channel flow problem.

The validation process is also performed for the 2D periodic hill flow case. It is determined to evaluate the finite-difference gradients at the inlet and mid-section of the flow domain. Seven different points of interest in y-direction are selected at each x-location for the validation process. Figure 8.3 illustrates the validation of the adjoint sensitivities through the finite-difference gradients for the selected evaluation locations in the 2D periodic hill flow case. It is shown that the relative errors between two approaches lie below 5% of the finite-difference gradients. Overall, the adjoint sensitivities agree with the finite-difference gradients.

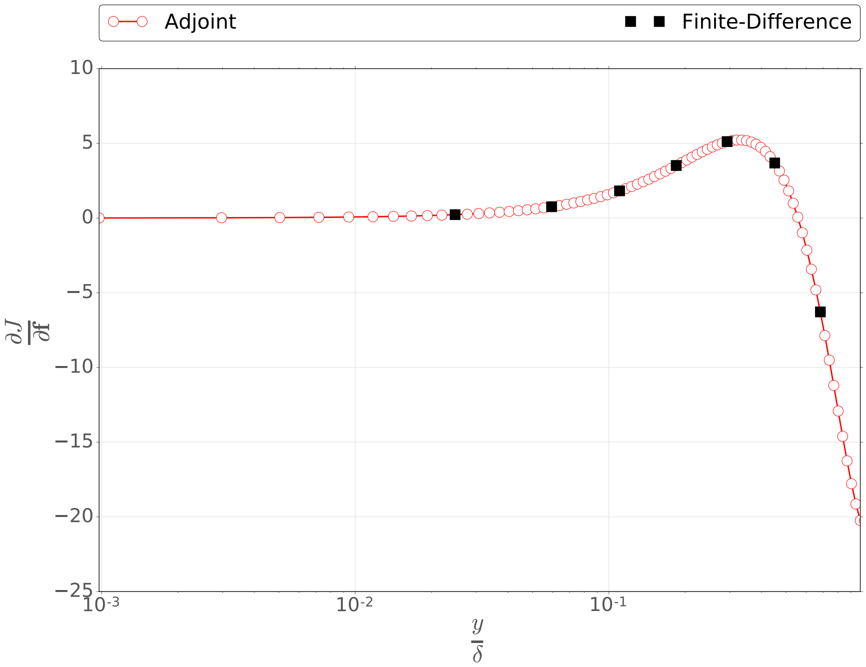

Figure 8.2: Validation of adjoint sensitivities on finite-difference gradients for the 1D channel flow case

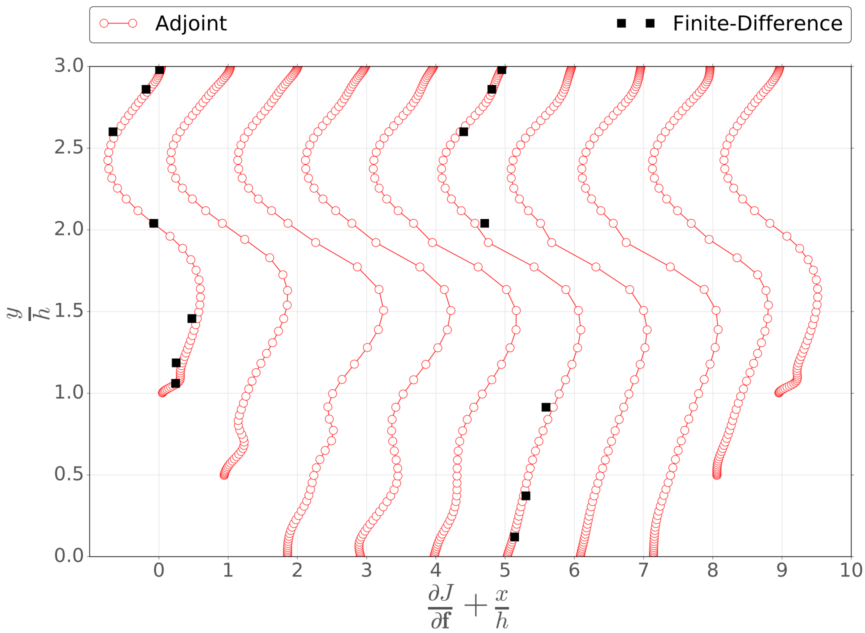

Figure 8.3: Validation of adjoint sensitivities on finite-difference gradients for the 2D periodic-hill case

An additional validation process is performed on the adjoint framework where the *frozen turbulence* assumption is used. Taylor (1938) addresses the idea of the *frozen turbulence* by considering the spatial structure of a turbulent velocity field from the a single point calculation or measurement of the temporal fluctuation as an actual structure of turbulence. The *frozen turbulence* assumption is useful for deriving the adjoint formulations because it allows to consider the eddy viscosity μ_t as independent to the flow variables. Considering a momentum equation where a design force $\mathbf{s}$ is added to the RANS momentum equation such that

$$\rho\nabla \cdot (\bar{\mathbf{u}}\bar{\mathbf{u}}) + \nabla\bar{p} - \nabla \cdot ((\mu + \mu_t)D(\bar{\mathbf{u}})) + \mathbf{s} = 0 \tag{8.1}$$

Following the derivation from Section 3.5, the adjoint momentum equation for (8.1) can be derived as

$$\nabla \cdot \rho\bar{\mathbf{u}} + (\rho\bar{\mathbf{u}} \cdot \nabla)\mathbf{v} + \nabla \cdot 2(\mu + \mu_t)D(\mathbf{v}) - \rho\nabla q + \sigma(\bar{\mathbf{u}} - \bar{\mathbf{u}}_{\mathbf{d}}) = 0 \tag{8.2}$$

$$\nabla \cdot \mathbf{v} = 0 \tag{8.3}$$

with a integral form of its adjoint boundary condtion

$$\begin{aligned} \int_\Gamma &(2(\mu + \mu_t)\mathbf{n} \cdot D(\delta\bar{\mathbf{u}})) \cdot \mathbf{v} + \delta\bar{p}(\mathbf{v} \cdot \mathbf{n}) + \\ &\delta\bar{\mathbf{u}} \cdot (\mathbf{n}(\mathbf{v} \cdot \rho\bar{\mathbf{u}}) + \mathbf{v}(\rho\bar{\mathbf{u}} \cdot \mathbf{n}) + 2(\mu + \mu_t)\mathbf{n} \cdot D(\mathbf{v}) - q\mathbf{n} + \sigma(\bar{\mathbf{u}} - \bar{\mathbf{u}}_{\mathbf{n}}))\, d\Gamma = 0 \end{aligned} \tag{8.4}$$

The validation process for the adjoint sensitivities based on (8.2) and (8.3) is performed on the 1D channel flow case.

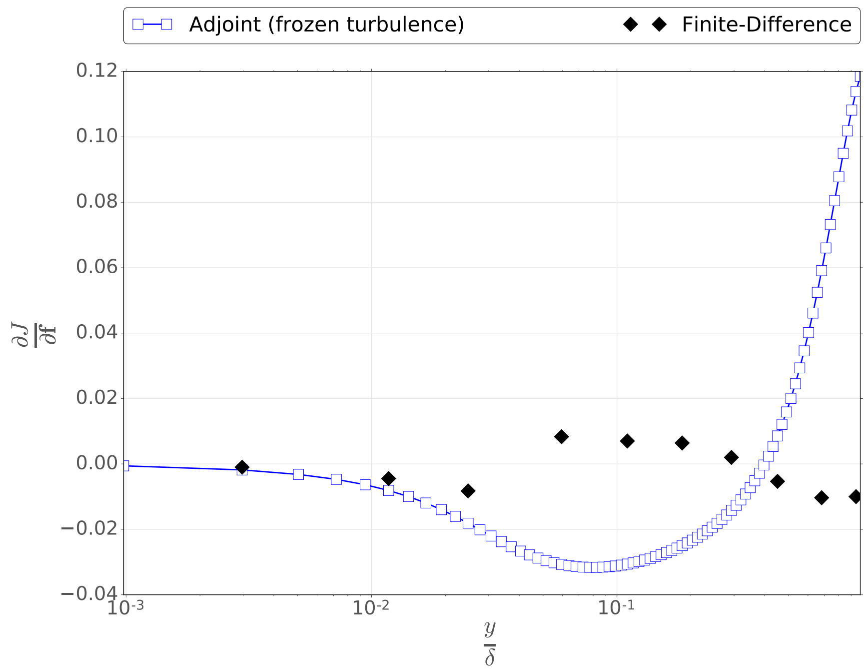

Figure 8.4: Influence of the *frozen turbulence* assumption on adjoint sensitivities for the 1D channel flow case

The adjoint sensitivities involving the *frozen turbulence* assumption are compared to the finite-difference gradients in Figure 8.4. In contrast to the previous validation results where the *frozen turbulence* assumption is not considered, the adjoint sensitivities do not match with the finite-difference gradients. The errors become enlarged as the evaluation point is further away from the wall. It can be seen that the continuous adjoint approach is disturbed by the *frozen turbulence* assumption at least in the framework of (8.1). As a result, the cost function J constrained by (8.1) will not be successfully minimized due to the invalid adjoint sensitivity computation.

Chapter 9

Conclusions and Recommendations

The objective of this thesis is to identify the momentum forcing $\mathbf{f}$ necessary to reduce the errors of the selected base-model in wall-bounded test cases by applying the full-field inversion approach and to determine whether the Reynolds stress tensor components can be identified using the mean DNS velocity vector field. As a final chapter of the thesis, the conclusions and recommendations will be addressed.

9.1 Conclusions

The literature study on existing RANS error estimation techniques concludes two major approaches. The Bayesian approach improves the RANS predictions by calibrating the closure coefficients of the RANS models. The turbulence production is iteratively corrected based on the estimated functional errors by the full-field inversion. However, since both approaches still rely on the Boussinesq assumption, they do not provide the improvement where the turbulent anisotropy plays a role.

The base-model momentum equation (2.31) is constructed to avoid the violation of the Boussinesq assumption by replacing the divergence of the Reynolds stress tensor with the momentum forcing $\mathbf{f}$. The optimization problem is formulated using a cost function J based on Bayesian statistics. Through the cost function J, the velocity difference between the base-model simulation and the DNS data is minimized by performing the adjoint-based optimization.

The flow simulations are implemented in OpenFOAM and the quasi-Newton algorithm (L-BFGS-B) from the python library is used for the optimization. The full-field inversion is performed on 1D channel flow and 2D periodic hill flow. The results of the full-field inversion are summarized:

- The base-model velocity errors with respect to the mean DNS velocity data for both test cases are significantly reduced by identifying the momentum forcing $\mathbf{f} = \hat{\mathbf{f}}$.
- Total number of cost function J evaluations drastically increase with the increase in the Reynolds number.
- In the 1D channel flow case, the identified momentum forcing $\hat{\mathbf{f}}$ mostly agrees with the DNS turbulence force profile except for the flow domain of $y^+ < 10$.
- At $y^+ \geq 30$, the identified momentum forcing $\hat{\mathbf{f}}$ experiences low-frequency oscillations for the 1D channel flow case.
- The extracted shear stress from $\hat{\mathbf{f}}$ strongly agrees with the DNS Reynolds shear stress data for the 1D channel flow case.
- The flow separation and reattachment locations are correctly estimated by the full-field inversion for the 2D periodic hill flow case.
- In the 2D periodic hill flow case, the identified momentum forcing $\hat{\mathbf{f}}$ deviates from the DNS turbulence force profiles due to the influence of the flow separation and the same applies to the shear stress comparison.
- The adjoint sensitivities used for the optimization are validated through the finite-different gradients for both test cases.

To sum up, the optimal momentum forcing $\hat{\mathbf{f}}$ is identified to reduce the base-model errors in both wall-bounded flow cases based on the mean DNS velocity data. The Reynolds shear stress can be identified using only the mean DNS velocity data for the 1D channel flow case. This is enabled by resulting a fully determined problem where the shear stress can be directly obtained from $\hat{\mathbf{f}}$ in the 1D channel flow problem. On the other hand, the identified shear stress for the 2D periodic hill flow case does not fully correspond to the DNS Reynolds shear stress data. The 2D periodic hill flow case results in the underdetermined problem where the direct identification of the Reynolds shear stress is no longer possible, thus using a minimization approach. This influences the result for the identified shear stress.

9.2 Recommendations

The full-field inversion in this thesis is currently applied for relatively low Reynolds number flow cases. It is observed that the increase of the Reynolds number leads to the significant increase in the total number of cost function evaluations. Accordingly, applying this framework for higher Reynolds number flow cases are obligate to perform further investigations on grid resolutions, numerical schemes and optimization algorithms to reduce the computational burden.

The low-frequency oscillations are observed in the optimal momentum forcing profile $\hat{\mathbf{f}}$ for the 1D channel flow case. They are considered as physical observations in this work as they are not influenced by the different numerical set-up. Further research can be conducted to characterize the observed oscillations and also to determine their impact on the velocity fields.

In the 2D periodic hill flow case, the wall shear stress at the inlet and the outlet of the flow domain was not correctly estimated through the full-field inversion. This is because the cost function is constructed to minimize the difference in the velocity fields. A better estimate of the wall shear stress can be obtained by constructing a new cost function which involves the wall shear stress as well as the velocity.

From the adjoint sensitivity validation, it is observed that the base-model framework (2.31) has provided the valid adjoint sensitivities. On the other hand, the framework where the eddy viscosity is still involved computes the adjoint sensitivities that do not agree with the finite-difference gradients. One possible cause of the invalid adjoint sensitivities is the *frozen turbulence* assumption. Hence, an additional investigation can be performed to analyse the influence of the *frozen turbulence* assumption either on continuous or discrete adjoint methods.

The framework has provided the capability of predicting velocity vector fields for the canonical wall-bounded test cases. The reconstruction of the velocity vector fields can be performed based on the limited sparse data points. The success of the sparse data reconstruction will increase the value of existing data from point measurement experiments such as Hot-Wire Anemometry. In addition, the framework has also enabled the possibility of getting information on the Reynolds shear stress by only having velocity information in the cost function. This also needs further research with the sparse data, which will be the next step from this thesis onwards.

Bibliography

Advanced Navigation and Control Systems Laboratory. Log error vs. log step size plot for geometric integration page, 2012. URL http://ancs.eng.buffalo.edu/index.php/File:Step_size.png#file. [Online; accessed January 10, 2017].

John D. Anderson. *Introduction to Flight, Section 4.20 (5th edition)*. McGraw-Hill Science Engineering, 2004. ISBN 9780072990713.

M. Breuer, N. Peller, Ch. Rapp, and M. Manhart. Flow over periodic hills numerical and experimental study in a wide range of reynolds numbers. *Computers & Fluids*, 38(2):433 – 457, 2009. ISSN 0045-7930. doi: http://dx.doi.org/10.1016/j.compfluid.2008.05.002. URL //www.sciencedirect.com/science/article/pii/S0045793008001126.

Sai Hung Cheung, Todd A. Oliver, Ernesto E. Prudencio, Serge Prudhomme, and Robert D. Moser. Bayesian uncertainty analysis with applications to turbulence modeling. *Reliability Engineering and System Safety*, 96(9):1137–1149, 2011. ISSN 0951-8320. doi: http://dx.doi.org/10.1016/j.ress.2010.09.013. URL http://www.sciencedirect.com/science/article/pii/S0951832011000664. Quantification of Margins and Uncertainties.

Olivier Cleynen. Fluid mechanics for masters students, 2016. URL https://documents.ariadacapo.net/cours/fluidmech/.

Nicolas Dovetta. *Data-based models for flow control*. Theses, Ecole Polytechnique X, June 2014. URL https://hal-polytechnique.archives-ouvertes.fr/tel-01097717.

Bernardo Alan de Freitas Duarte, Isabella Cristina Resende Ramos, and HersÃlia de Andrade e Santos. Reynolds shear-stress and velocity: positive biological response of neotropical fishes to hydraulic parameters in a vertical slot fishway. *Neotropical Ichthyology*, 10: 813 – 819, 10 2012. ISSN 1679-6225.

Richard P. Dwight and Joël Brezillon. *Adjoint Algorithms for the Optimization of 3d Turbulent Configurations*, pages 194–201. Springer Berlin Heidelberg, Berlin, Heidelberg, 2008. ISBN 978-3-540-74460-3. doi: 10.1007/978-3-540-74460-3_24. URL http://dx.doi.org/10.1007/978-3-540-74460-3_24.

W.N. Edeling, P. Cinnella, R.P. Dwight, and H. Bijl. Bayesian estimates of parameter variability in the $k - \epsilon$ turbulence model. *Journal of Computational Physics*, 258:73 – 94, 2014. ISSN 0021-9991. doi: http://dx.doi.org/10.1016/j.jcp.2013.10.027. URL http://www.sciencedirect.com/science/article/pii/S0021999113007031.

Michael Emory, Rene Pecnik, and Gianluca Iaccarino. Modeling structural uncertainties in reynolds-averaged computations of shock/boundary layer interactions, 2011. URL http://dx.doi.org/10.2514/6.2011-479. 49th AIAA Aerospace Sciences Meeting including the New Horizons Forum and Aerospace Exposition.

Dimitry P. G. Foures, Nicolas Dovetta, Denis Sipp, and Peter J. Schmid. A data-assimilation method for reynolds-averaged navierstokes-driven mean flow reconstruction. *Journal of Fluid Mechanics*, 759:404–431, 11 2014. doi: 10.1017/jfm.2014.566.

C. Gorlé and G. Iaccarino. A framework for epistemic uncertainty quantification of turbulent scalar flux models for reynolds-averaged navier-stokes simulations. *Physics of Fluids*, 25(5): 055105, 2013. doi: 10.1063/1.4807067. URL http://dx.doi.org/10.1063/1.4807067.

C. Gorlé, M. Emory, J. Larsson, and G. Iaccarino. Epistemic uncertainty quantification for rans modeling of the flow over a wavy wall, 2012. Annual Research Briefs 2012.

Jason Hicken, Prof. Juan Alonso, and Prof. Charbel Farhat. Lecture notes in multidisciplinary design optimization, 2012.

C. Hinterberger and M. Olesen. Industrial application of continuous adjoint flow solvers for the optimization of automotive exhaust systems. *ECCOMAS Thematic Conference*, 2011.

Gianluca Iaccarino. Lecture notes in computational methods in fluid dynamics using commercial cfd codes, 2004.

M.C. Kennedy and A. OHagan. Bayesian calibration of computer models. *Journal of the Royal Statistical Society: Series B (Statistical Methodology)*, 63(3):425464, 2001.

B.E. Launder and B.I. Sharma. Application of the energy-dissipation model of turbulence to the calculation of flow near a spinning disc. *Letters in Heat and Mass Transfer*, 1(2):131 – 137, 1974. ISSN 0094-4548. doi: http://dx.doi.org/10.1016/0094-4548(74)90150-7. URL http://www.sciencedirect.com/science/article/pii/0094454874901507.

Brian E. Launder. First steps in modelling turbulence and its origins: a commentary on reynolds (1895) 'on the dynamical theory of incompressible viscous fluids and the determination of the criterion'. *Philosophical Transactions of the Royal Society of London A: Mathematical, Physical and Engineering Sciences*, 373(2039), 2015. ISSN 1364-503X. doi: 10.1098/rsta.2014.0231. URL http://rsta.royalsocietypublishing.org/content/373/2039/20140231.

Myoungkyu Lee and Robert D. Moser. Direct numerical simulation of turbulent channel flow up to $\mathcal{R}e_\tau \approx 5200$. 774:395–415, 007 2015. doi: 10.1017/jfm.2015.268.

M. Leschziner. *Statistical Turbulence Modelling for Fluid Dynamics, Demystified: An Introductory Text for Graduate Engineering Students*. 2015. ISBN 9781783266623.

R. LeVeque. *Finite Difference Methods for Ordinary and Partial Differential Equations*. Society for Industrial and Applied Mathematics, 2007. doi: 10.1137/1.9780898717839. URL http://epubs.siam.org/doi/abs/10.1137/1.9780898717839.

F. Moukalled, L. Mangani, and M. Darwish. *The Finite Volume Method in Computational Fluid Dynamics: An Advanced Introduction with OpenFOAM and Matlab*. Springer Publishing Company, Incorporated, 1st edition, 2015. ISBN 3319168738, 9783319168739.

Siva Nadarajah and Antony Jameson. Studies of the continuous and discrete adjoint approaches to viscous automatic aerodynamic shape optimization. *15th AIAA Computational Fluid Dynamics Conference*, 2001. URL http://dx.doi.org/10.2514/6.2001-2530.

J. Nocedal and S. J. Wright. *Numerical Optimization*. Springer, New York, 2nd edition, 2006.

Todd A Oliver and Robert D Moser. Bayesian uncertainty quantification applied to rans turbulence models. *Journal of Physics: Conference Series*, 318(4):042032, 2011. URL http://stacks.iop.org/1742-6596/318/i=4/a=042032.

C. Othmer. A continuous adjoint formulation for the computation of topological and surface sensitivities of ducted flows. *International Journal for Numerical Methods in Fluids*, 58 (8):861–877, 2008. ISSN 1097-0363. doi: 10.1002/fld.1770. URL http://dx.doi.org/10.1002/fld.1770.

Ronald L. Panton. *Incompressible Flow*. John Wiley & Sons, Inc., 2013. ISBN 9781118713075. doi: 10.1002/9781118713075.ch8. URL http://dx.doi.org/10.1002/9781118713075.ch8.

Eric Parish and Karthik Duraisamy. *Quantification of turbulence modeling uncertainties using full field inversion*. American Institute of Aeronautics and Astronautics Inc, AIAA, 2015. ISBN 9781624103667.

Eric J. Parish and Karthik Duraisamy. A paradigm for data-driven predictive modeling using field inversion and machine learning. *Journal of Computational Physics*, 305:758 – 774, 2016. ISSN 0021-9991. doi: http://dx.doi.org/10.1016/j.jcp.2015.11.012. URL http://www.sciencedirect.com/science/article/pii/S0021999115007524.

Stephen B. Pope. *Turbulent Flows*. Cambridge University Press, 2000. ISBN 9780511840531. URL http://dx.doi.org/10.1017/CBO9780511840531. Cambridge Books Online.

B. Borchers R. C. Aster and C. H. Thurber. *Parameter Esimation and Inverse Problems*. Elsevier academic press, 2005. ISBN 0-12-065604-3.

P.J. Roache. *Verification and Validation in Computational Science and Engineering*. Hermosa, 1998. ISBN 9780913478080.

Anand Pratap Singh and Karthik Duraisamy. Using field inversion to quantify functional errors in turbulence closures. *Physics of Fluids*, 28(4):045110, 2016. doi: http://dx.doi.org/10.1063/1.4947045. URL http://scitation.aip.org/content/aip/journal/pof2/28/4/10.1063/1.4947045.

A. Tarantola. *Inverse Problem Theory and Methods for Model Parameter Estimation*. Society for Industrial and Applied Mathematics, 2005. doi: 10.1137/1.9780898717921. URL http://epubs.siam.org/doi/abs/10.1137/1.9780898717921.

G. I. Taylor. The spectrum of turbulence. *Proceedings of the Royal Society of London A: Mathematical, Physical and Engineering Sciences*, 164(919):476–490, 1938. ISSN 0080-4630. doi: 10.1098/rspa.1938.0032. URL http://rspa.royalsocietypublishing.org/content/164/919/476.

Q. Wang and E. A. Dow. Quantification of structural uncertainties in the $k - \epsilon$ turbulence model. *AIAA Paper 2011*, 1762, 2011.

Carl Wunsch. *The ocean circulation inverse problem.* Cambridge university press, 1997.

H. Xiao, J.-L. Wu, J.-X. Wang, R. Sun, and C.J. Roy. Quantifying and reducing model-form uncertainties in reynolds-averaged navierstokes simulations: A data-driven, physics-informed bayesian approach. *Journal of Computational Physics*, 324:115 – 136, 2016. ISSN 0021-9991. doi: http://dx.doi.org/10.1016/j.jcp.2016.07.038. URL http://www.sciencedirect.com/science/article/pii/S0021999116303394.